Sublattice symmetry breaking and Kondo-effect enhancement in strained graphene

Dawei Zhai,[1] Kevin Ingersent,[2] Sergio E. Ulloa,[1] and Nancy Sandler[1]

[1]*Department of Physics and Astronomy, and Ohio Materials Institute, Ohio University, Athens, Ohio 45701-2979, USA*
[2]*Department of Physics, University of Florida, P.O. Box 118440, Gainesville, Florida 32611-8440, USA*

Kondo physics in doped monolayer graphene is predicted to exhibit unusual features due to the linear vanishing of the pristine material's density of states at the Dirac point. Despite several attempts, conclusive experimental observation of the phenomenon remains elusive. One likely obstacle to identification is a very small Kondo temperature scale T_K in situations where the chemical potential lies near the Dirac point. We propose tailored mechanical deformations of monolayer graphene as a means of revealing unique fingerprints of the Kondo effect. Inhomogeneous strains are known to produce specific alternating changes in the local density of states (LDOS) away from the Dirac point that signal sublattice symmetry-breaking effects. Small LDOS changes can be amplified in an exponential increase or decrease of T_K for magnetic impurities attached at different locations. We illustrate this behavior in two deformation geometries: a circular "bubble" and a long fold, both described by Gaussian displacement profiles. We calculate the LDOS changes for modest strains and analyze the relevant Anderson impurity model describing a magnetic atom adsorbed in either a "top-site" or a "hollow-site" configuration. Numerical renormalization-group solutions of the impurity model suggest that higher expected T_K values, combined with distinctive spatial patterns under variation of the point of graphene attachment, make the top-site configuration the more promising for experimental observation of signatures of the Kondo effect. The strong strain sensitivity of T_K may lift top-site Kondo physics into the range experimentally accessible using local probes such as scanning tunneling microscopy.

I. INTRODUCTION

The honeycomb structure of the graphene lattice has interesting consequences for the low-energy electron dynamics. An effective massless dispersion near the Dirac point, accompanied by spinor eigenstates with well-defined helicities that impose specific phase relations between their components, yields high carrier mobilities and unique optical properties for the pristine material [1]. In addition, the strong sp^2 carbon bonding confers remarkable mechanical properties that allow graphene to withstand high levels of in-plane strain while being easily rippled under external stress, much like paper [2]. The formation of wrinkles [3–5], folds [6–8], and bubbles [9] can be driven by lattice mismatch with a substrate [10,11], intercalated impurities trapped during the deposition process [12], or directly by external application of controlled stress fields [13].

Such local deformations of graphene are responsible for inhomogeneous charge density distributions with characteristics determined by the magnitude and spatial dependence of the strain field. The connection between deformations and charge inhomogeneities was quantitatively confirmed in recent measurements of the local density of states (LDOS) via scanning tunneling microscopy (STM) in setups with mobile (tip-induced) and static (intercalated impurity) local deformations [14]. Analysis of STM images revealed local sublattice symmetry breaking in strained regions, whereby the two carbon atoms within each unit cell are differentiated by contrasting signal intensities. Interestingly, despite the local deformation, the gapless dispersion of the pristine sample is maintained. Strain-induced density enhancements have also been reported in transport experiments through isolated folds, where charge confinement gives rise to Coulomb-blockade features across the axis of the fold [15].

The studies cited in the previous paragraph suggest that strain may be used to control local charge distributions and thereby reach regimes where electron-electron interactions are important that are difficult to access in undeformed graphene. An iconic example of strong correlations is the Kondo effect, where mobile carriers collectively screen a localized magnetic moment embedded in the system. This many-body phenomenon depends on the dynamics of spin carriers and is sensitive to magnetic fields [16]. Its characteristic energy scale, set by the Kondo temperature T_K, depends strongly on both the hybridization matrix elements between localized and delocalized levels and the LDOS of delocalized levels at the local-moment site. Pristine graphene is predicted to be the setting for two distinct types of Kondo physics. If the material is doped or gated so that its chemical potential is away from the Dirac point, the Kondo effect is expected to be largely conventional: the impurity contribution to bulk properties should show the same dependencies at sufficiently low temperatures, frequencies, and magnetic fields as are found in a three-dimensional bulk metal [16]. In undoped graphene, where the chemical potential lies precisely at the Dirac point, theory instead predicts [17–19] a "pseudogap" Kondo effect [20] with very different low-energy properties [19,21–28]. In both the conventional and pseudogap cases, clear evidence for the Kondo effect can be obtained only in experiments that are able to probe temperatures below T_K.

Kondo physics has recently been proposed to be the origin of features in angle-resolved photoemission on Ce-intercalated graphene [29]. However, the experimental setups most commonly pursued to realize the Kondo effect in graphene involve either vacancies in the carbon lattice or adatoms deposited on top of the sample. Claims of definitive detection of Kondo physics in these settings remain controversial. Magnetotransport measurements on irradiated (vacancy containing) graphene appear to reproduce the characteristic temperature dependence of the resistivity [30], but doubt has been cast on the Kondo interpretation by (i) the persistence of this dependence as the chemical potential was tuned through the Dirac point [26], and (ii) the absence of Kondo signatures in the magnetic response of irradiated graphene [31] (although see [32]). More recently, graphene with isolated vacancies has been reported to exhibit Kondo features [33] with a crucial dependence on curvature of the graphene sheet [34].

Local STM probes of adatoms on graphene have yielded even more ambiguous results. For example, early studies of cobalt adatoms on graphene found features in the conductance expected for single- and two-channel Kondo effects, associating the two cases with different adsorption geometries [35]. However, similar features were later suggested to arise instead from inelastic tunneling mediated by vibrations of cobalt adatoms [36]. STM experiments involving hydrogen or fluorine adsorbed on graphene have revealed no Kondo signatures [37], although different possible gating and/or doping regimes have not yet been fully explored.[1]

First-principles prediction of the properties of adatoms on graphene has also proved to be very challenging. An STM study of preferred adsorption sites for nickel and cobalt adatoms on graphene with different substrate conditions [38] in some cases bore out, and in others contradicted, the predictions of density-functional theory. Theoretical analyses [24,39,40] suggest that the STM signatures of adatoms on graphene are highly sensitive to the absorption geometry, which determines the relative energies of different atomic orbitals, the effective Coulomb interactions between electrons in various adatom orbitals, and the overlap integrals between adatom and host orbitals. The Berry phase associated with the two inequivalent Dirac points has also been predicted to play an essential role [39].

It has been argued that part of the difficulty with observing the Kondo effect with adatoms on graphene is the low density of states near the Dirac point, which is expected to strongly suppress the Kondo temperature of the system [23,25–27] (especially for cases of strict particle-hole symmetry, where no Kondo screening is possible [22,25,26]). Clear identification of Kondo features may also be hindered by long-range charge fluctuations producing a distribution of Kondo temperatures [41] and by the spatial delocalization of the impurity magnetic moment over nanometer scales [37].

Recent experiments on graphene deposited on Ru(0001) surfaces [42] have highlighted strain as an important factor. Lattice mismatch with the substrate imparts a rippled moiré superstructure to graphene. Cobalt atoms were seen to adhere preferentially to graphene regions of high strain. Fits of the

differential conductance to Fano line shapes suggested different Kondo temperatures $T_K \simeq 12$ and 5 K for adsorption at two types of site, each located at a local maximum of the strain. The Kondo interpretation was supported by the observation of magnetic-field-induced Zeeman splitting of the zero-bias conductance feature. Although these results appear to provide strong evidence for Kondo physics, it is hard to point to this as an example of Kondo screening by pristine graphene since strong hybridization with Ru(0001) surface states washes out the Dirac point and its linear dispersion [43].

We propose that with suitable modifications, experiments like those in Ref. [42] are very promising for the observation and characterization of unique features of Kondo physics in graphene. The key idea is to study samples in which the strained regions are not strongly hybridized with a substrate. This may be accomplished by employing a substrate such as hBN, or by focusing on free-standing graphene. In this paper, we show that smooth deformations can induce modest modulations of the LDOS that lead to strong changes in the Kondo temperature when the chemical potential lies in the linear dispersion regime near, but not precisely at, the Dirac point. The LDOS modulations consist of two components: one that breaks particle-hole symmetry about the Dirac point, and one that breaks the symmetry between sublattices A and B. In certain regions near a deformation, an increase in the LDOS of one sublattice is accompanied by a reduction of the LDOS at nearby sites of the other sublattice. This local sublattice symmetry breaking is amplified in the dependence of the Kondo temperature on the location at which a magnetic atom adsorbs to the graphene host. In some cases, an exponential enhancement of the Kondo scale will allow the observation of Kondo physics where it would be undetectable in the absence of deformation.

We illustrate these ideas for two representative out-of-plane deformation geometries: a localized Gaussian "bubble" with circular symmetry and an extended Gaussian "fold" that preserves lattice translational symmetry along the fold axis. We present and apply a formalism for calculating the graphene LDOS changes resulting from modest strains, then analyze the relevant Anderson impurity model describing a magnetic atom in one or other of the two most probable adsorption configurations: so-called "top" and "hollow" sites. Through nonperturbative numerical renormalization-group calculations, we demonstrate that top-site adsorption above a single carbon atom leads to strong strain sensitivity: even weak deformations (strain $\lesssim 1\%$) can result in enhancement of T_K by at least an order of magnitude. For hollow-site adsorption at the center of a carbon hexagon, it is unlikely that modest strains can overcome a strong suppression of the Kondo scale in prsitine graphene that results from destructive interference between tunneling of electrons between the adatom and the six nearest host atoms.

The organization of the remainder of the paper is as follows. Section II reviews a description of strained graphene in terms of scalar and (pseudo)vector gauge fields. This formalism is applied to compute the LDOS near a Gaussian bubble and a Gaussian fold. Section III presents Anderson impurity models describing top-site adsorption and hollow-site adsorption of a magnetic atom and emphasizes the differing effects of strain in the two configurations. Numerical solutions of the

---

[1]I. Brihuega (private communication).

impurity model are used to map the variation of the Kondo temperature with the location of top-site adsorption near a Gaussian bubble or a Gaussian fold. Section IV discusses the results and presents suggestions for experimental conditions favorable for the observation of the predicted features.

II. LDOS OF STRAINED GRAPHENE

A successful way to describe strain in graphene within a continuum Hamiltonian formulation is by introducing effective (pseudo)gauge fields that change electron dynamics without breaking time-reversal symmetry [44,45]. Deformation-induced changes in the LDOS can be understood in terms of (pseudo) Landau levels [12] or long-lived local resonances (quasibound states) that are strain-field dependent [8,15]. Due to the space inversion symmetry properties of the gauge fields, strain is predicted to produce valley-filtered currents where electrons near the two Dirac points are scattered differentially [14,46]. These effects are expected to be enhanced in the presence of external electromagnetic fields [47].

This section reviews aspects of the continuum description of strained graphene and presents calculations of the LDOS at points near out-of-plane Gaussian deformations. Since such deformations have been the topic of several previous studies [46,48–52], Sec. II A presents a unified framework to enable comparison between various results. The framework facilitates a discussion of various effects introduced by strain and identifies those captured in scalar and pseudovector fields as most relevant for electron dynamics in the energy range of interest. Section II B outlines the Green's function formalism used to calculate the LDOS in deformed graphene. Based on underlying lattice symmetries of graphene and the effective gauge fields, we derive relations between deformation-induced changes in the LDOS in each valley and on each sublattice. These relations point to the origins of the sublattice symmetry breaking and particle-hole symmetry breaking that are evident in the LDOS and, furthermore, are shown in Sec. III to be magnified in the spatial variation of the Kondo temperature scale. The section concludes by illustrating the LDOS at different spatial positions relative to a Gaussian bubble or fold, as calculated for several representative combinations of model parameters.

A. Strain represented via effective gauge fields

We start with a model for undistorted monolayer graphene, with nearest-neighbor bond length $a = 1.42$ Å, assumed to lie in the plane $z = 0$ with the x (y) axis chosen to point along one of the zigzag (bond) directions. Throughout this paper, boldface symbols represent two-dimensional vectors in the x-y plane, and indices i, j run over 1 and 2 (equivalent to x and y, respectively).

Deformations of the two-dimensional graphene membrane that are smooth on interatomic length scales can be described within continuum elasticity theory. In-plane and out-of-plane displacements of carbon atoms from their equilibrium positions are assumed to be described by functions $\mathbf{u}(\mathbf{r})$ and $h(\mathbf{r})$, respectively, that vary slowly with undistorted in-plane position $\mathbf{r} = (x, y) \equiv (r\cos\phi, r\sin\phi)$. To lowest order, the

deformation is described by an in-plane strain tensor [53]

$$\epsilon_{ij} = \tfrac{1}{2}(\partial_j u_i + \partial_i u_j + \partial_i h \partial_j h). \tag{1}$$

One effect of the deformation is to replace an undistorted nearest-neighbor lattice vector $\boldsymbol{\delta}$ by a distorted counterpart $\boldsymbol{\delta}'$ of length [54,55]

$$|\boldsymbol{\delta}'| = a + \frac{1}{a}\boldsymbol{\delta} \cdot \epsilon \cdot \boldsymbol{\delta}. \tag{2}$$

As a result, the undistorted nearest-neighbor hopping matrix element t_0 changes to [56]

$$\begin{aligned} t &= t_0 \exp[-\beta(|\boldsymbol{\delta}'|/a - 1)] \\ &\simeq t_0[1 - (\beta/a^2)\boldsymbol{\delta} \cdot \epsilon \cdot \boldsymbol{\delta}], \end{aligned} \tag{3}$$

where $\beta \simeq 3$ is the Grüneisen parameter [57].

The modified hopping can be inserted into the nearest-neighbor tight-binding Hamiltonian describing the π electrons in graphene. Linearization around the Dirac points K and K' yields a low-energy (effective) Hamiltonian for deformed graphene that, when written in the valley-isotropic basis (K_A, K_B) and $(-K'_B, K'_A)$ [58], can be expressed in the form

$$H_\tau = v_F \boldsymbol{\sigma} \cdot [-i\hbar\nabla - \tau\mathbf{K} + \tau e\mathbf{A}(\mathbf{r})] + \Phi(\mathbf{r})\sigma_0. \tag{4}$$

Here, $\tau = 1\,(-1)$ identifies the K (K') valley centered around wave vector $\tau\mathbf{K}$ with $\mathbf{K} = (4/3^{3/2}, 0)\pi/a$, $-e$ is the electron charge, $v_F = 3t_0 a/2\hbar$ is the Fermi velocity, which we take to be $v_F = 10^6$ m/s (implying that $t_0 = 3.1$ eV); σ_x and σ_y are Pauli matrices, and σ_0 is the 2×2 identity matrix, all acting on the sublattice index. The effect of the deformation is contained in effective gauge fields [45,59]: a vector potential $\mathbf{A}$ having components

$$A_x = \frac{\hbar\beta}{2ea}(\epsilon_{yy} - \epsilon_{xx}), \quad A_y = \frac{\hbar\beta}{ea}\epsilon_{xy}, \tag{5}$$

and a scalar potential

$$\Phi(\mathbf{r}) = g_s(\epsilon_{xx} + \epsilon_{yy}). \tag{6}$$

Equation (4) takes the form of the Hamiltonian for free electrons in the presence of an electric field $\mathbf{E} = -\nabla\Phi$ and a pseudomagnetic field $\mathbf{B} = \nabla \times (\tau\mathbf{A})$. The pseudomagnetic field changes signs between valleys, locally breaking the underlying inversion symmetry of the honeycomb lattice but preserving time-reversal invariance. This sign reversal gives $\tau\mathbf{A}$ the character of a *pseudovector* gauge field.

The existence of a scalar potential of the form of Eq. (6) was originally argued [59] in the context of carbon nanotubes, based on preservation of charge neutrality in a deformed area, and led to an unambiguous prediction that $g_s > 0$. The value of g_s for graphene has been reported to be between 4 and 6 eV [45,57]. However, one well-cited study corresponds to $g_s = -2.5$ eV [60] and another may be interpreted as giving a similar value [61]. Given this uncertainty over the sign of g_s, below we illustrate results obtained both for positive and negative values of g_s.

In this work, we consider setups where the deformations are of low aspect ratio, i.e., the maximum out-of-plane displacement is much smaller than the in-plane distance over which the deformation occurs. These conditions can be created, for example, when atoms or molecules are intercalated
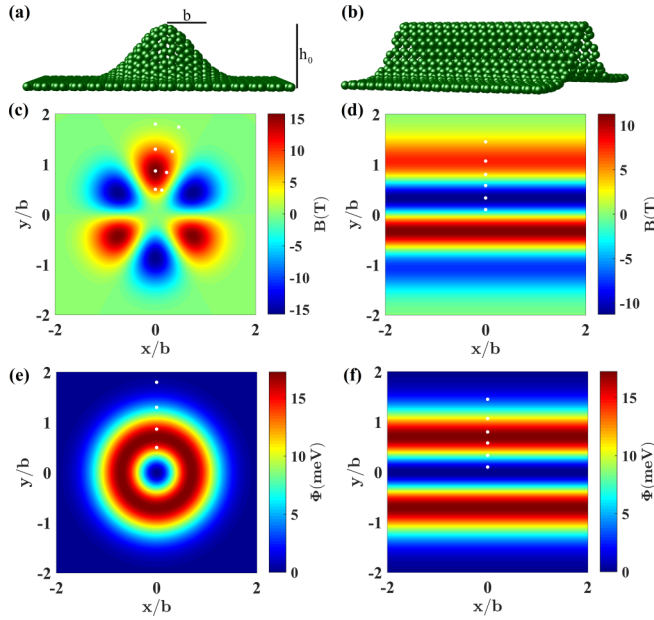
FIG. 1. Two types of out-of-plane Gaussian deformation studied in this work: (a) a circular bubble and (b) a long fold. Below each schematic is a corresponding color map of (c), (d) the effective magnetic field B for electrons in the K valley, and (e), (f) the scalar potential Φ near both K and K'. White circles in (c)–(f) indicate positions where the LDOS is plotted in Figs. 2 and 3. Data shown are for deformations of peak height $h_0 = 1$ nm and Gaussian half-width $b = 8$ nm, with couplings $g_v = 7$ eV and $g_s = 3$ eV.

between graphene and a substrate, or through substrate engineering [8,62]. In such cases, in-plane atomic displacements $\mathbf{u}(\mathbf{r})$ can be neglected compared to out-of-plane displacements $h(\mathbf{r})$ in Eq. (1) [2].

We focus on two specific deformation geometries: a circular "bubble" and a long "fold" extending along the x (zigzag) direction, both having Gaussian out-of-plane height profiles [46,49–52]. The bubble, shown schematically in Fig. 1(a), is a centrosymmetric deformation described in the Monge parametrization [63] by a height function

$$h(\mathbf{r}) = h_0 \, e^{-r^2/b^2}, \tag{7}$$

while the long fold, sketched in Fig. 1(b), has an out-of-plane profile

$$h(\mathbf{r}) = h_0 \, e^{-y^2/b^2}. \tag{8}$$

For these specific deformations, the description in terms of continuum elasticity theory is valid as long as we take $\eta = (h_0/b)^2 \ll 1$ [53], while the condition $b \gg a$ ensures the absence of intervalley scattering. Under both geometries, the strain field given by Eq. (1) is spatially inhomogeneous and has a peak magnitude $\epsilon_{\max} = \eta^2/e$ with e being Euler's number (not to be confused with the elementary positive charge e). All results presented in this paper are for deformations with a peak height $h_0 = 1$ nm and a Gaussian half-width $b = 8$ nm, for which the maximum strain takes a rather small value $\epsilon_{\max} \simeq 0.6\%$.

For the circular bubble, Eq. (5) predicts a vector potential

$$\mathbf{A}(\mathbf{r}) = \frac{g_v \eta^2}{e v_F} f\left(\frac{r}{b}\right) (-\cos 2\phi, \ \sin 2\phi), \tag{9}$$

where $g_v = \hbar \beta v_F / 2a \simeq 7$ eV and $f(z) = 2z^2 \exp(-2z^2)$, while Eq. (6) gives a scalar potential

$$\Phi(\mathbf{r}) = g_s \eta^2 f\left(\frac{r}{b}\right). \tag{10}$$

The corresponding gauge fields for the long fold are

$$\mathbf{A}(\mathbf{r}) = \frac{g_v \eta^2}{e v_F} f\left(\frac{y}{b}\right) (1, \ 0) \tag{11}$$

and

$$\Phi(\mathbf{r}) = g_s \eta^2 f\left(\frac{y}{b}\right). \tag{12}$$

Figures 1(c) and 1(d) map the effective out-of-plane magnetic field $B(\mathbf{r}) = \nabla \times \mathbf{A}(\mathbf{r}) = B(\mathbf{r}) \hat{\mathbf{z}}$ as experienced by electrons in the K valley. This field has the opposite sign for electrons in the K' valley. The effective field $B(\mathbf{r})$ produced by a circular bubble [Fig. 1(c)] exhibits threefold rotational symmetry about the deformation peak at $\mathbf{r} = \mathbf{0}$ with alternating positive and negative "petals," as previously reported [14,45,49,50]. The effective magnetic field created by a long fold [Fig. 1(d)] is odd under $y \to -y$ with alternating positive and negative regions on each side of the fold axis. By contrast, the corresponding scalar fields, mapped in Figs. 1(e) and 1(f), exhibit the even symmetry of the deformation profile.

Aside from the gauge fields described above, which originate in bond-length deformations, strain induces other effects: (1) Additional gauge fields arise from changes in the orientation of π orbitals as the graphene membrane is displaced out of the plane [64,65]. These fields can be shown to be smaller than those in Eqs. (5) and (6) by a multiplicative factor of order $(a/b)^2$. (2) Shifts in the positions of the K and K' points in reciprocal space lead to renormalization of the effective Fermi velocity v_F [45,61,66–69]. Based on Ref. [61], we estimate that this renormalization induces fractional LDOS changes $|\Delta \rho|/\rho \lesssim 4\epsilon_{\max}$. For the specific situations illustrated in this paper, where $(a/b)^2 \simeq 0.02$ and $\epsilon_{\max} = 0.6\%$, effects (1) and (2) can be safely neglected.

B. LDOS changes induced by strains

In the continuum limit, the LDOS at position $\mathbf{r}$ and energy E of electrons on sublattice $\ell = 1$ or 2 in valley $\tau = \pm 1$ is

$$\rho_{\tau,\ell}(\mathbf{r}, E) = -\pi^{-1} s_E \, \mathrm{Im}[G_\tau(\mathbf{r}, \mathbf{r}, E)]_{\ell\ell}. \tag{13}$$

Here, $s_E = \mathrm{sgn}\,E$ and $[G_\tau(\mathbf{r}, \mathbf{r}', E)]_{\ell\ell'}$, an element of the 2×2 matrix single-particle Green's function

$$G_\tau(\mathbf{r}, \mathbf{r}', E) = \langle \mathbf{r} | (E + i s_E 0^+ - H_\tau)^{-1} | \mathbf{r}' \rangle,$$
$$\equiv e^{i\tau \mathbf{K} \cdot (\mathbf{r} - \mathbf{r}')} \bar{G}_\tau(\mathbf{r}, \mathbf{r}', E) \tag{14}$$

describes propagation of an electron in valley τ from spatial location $\mathbf{r}'$ in sublattice ℓ' to location $\mathbf{r}$ in sublattice ℓ. The distinction between G_τ and $\bar{G}_\tau$, which is usually neglected and does not affect the density of states [Eq. (13)], will prove to be important when we consider hollow-site adsorption of a magnetic impurity (see Sec. III C).

In the limit $b \gg a$ considered in this work, the slowly varying deformation induces negligible intervalley scattering and one can calculate $G_\tau(\mathbf{r}, \mathbf{r}', E)$ perturbatively in the Born approximation [70] as

$$G_\tau(\mathbf{r}, \mathbf{r}', E) \simeq G_{0,\tau}(\mathbf{r}, \mathbf{r}', E) + \int G_{0,\tau}(\mathbf{r}, \mathbf{r}_1, E) [V_\tau(\mathbf{r}_1)$$
$$+ \Phi(\mathbf{r}_1)\sigma_0] G_{0,\tau}(\mathbf{r}_1, \mathbf{r}', E) d\mathbf{r}_1, \qquad (15)$$

where $G_{0,\tau}$ is the Green's function of pristine graphene, and the first and second terms in the square brackets describe scattering at a location $\mathbf{r}_1 = (x_1, y_1) \equiv (r_1 \cos\phi_1, r_1 \sin\phi_1)$ due to the effective vector and scalar potentials, respectively. When written in the valley-isotropic basis (K_A, K_B) and $(-K'_B, K'_A)$, $\bar{G}_{0,\tau} \equiv \bar{G}_0$ is independent of τ. Within the approximation of a linear dispersion in pristine graphene, i.e., $\varepsilon_\mathbf{k} = \pm \hbar v_F |\mathbf{k} - \tau\mathbf{K}|$ (valid for $|\varepsilon_\mathbf{k}| \ll t_0$), one can show [71] that

$$\bar{G}_0(\mathbf{r}, \mathbf{r}', E) = -\frac{iq}{4\hbar v_F} \begin{pmatrix} s_E H_0(qd) & ie^{-i\phi_d} H_1(qd) \\ ie^{i\phi_d} H_1(qd) & s_E H_0(qd) \end{pmatrix}. \quad (16)$$

Here, $q = |E|/\hbar v_F$, $H_n(x)$ is the order-n Hankel function of the first kind, and $\mathbf{d} = \mathbf{r} - \mathbf{r}' \equiv (d \cos\phi_d, d \sin\phi_d)$. After summation over the valley index, the pristine Green's function leads to a pristine density of states per sublattice, per spin orientation, and per unit area

$$\rho_0(E) = \frac{|E|}{2\pi \hbar^2 v_F^2}. \qquad (17)$$

For the Gaussian bubble, the scattering matrix arising from the pseudovector field $\tau\mathbf{A}(\mathbf{r})$ is

$$V_\tau(\mathbf{r}_1) = \tau e v_F \boldsymbol{\sigma} \cdot \mathbf{A}(\mathbf{r}_1)$$
$$= -\tau g_v \eta^2 f\left(\frac{r_1}{b}\right) \begin{pmatrix} 0 & e^{i2\phi_1} \\ e^{-i2\phi_1} & 0 \end{pmatrix}. \qquad (18)$$

The corresponding quantity for the Gaussian fold is

$$V_\tau(\mathbf{r}_1) = \tau g_v \eta^2 f\left(\frac{y_1}{b}\right) \begin{pmatrix} 0 & 1 \\ 1 & 0 \end{pmatrix}. \qquad (19)$$

Using Eqs. (10), (12), (15), (16), (18), and (19), and noting that the elements of the unperturbed Green's function satisfy

$$[G_0(\mathbf{r}, \mathbf{r}', E)]_{jj'} = (-1)^{j-j'+1}[G_0(\mathbf{r}, \mathbf{r}', -E)]_{jj'}$$
$$= (-1)^{j-j'}[G_0(\mathbf{r}', \mathbf{r}, E)]_{jj'} \qquad (20)$$

for $j, j' \in \{1, 2\}$, one can show that $\Delta G_\tau^v(\mathbf{r}, \mathbf{r}_1, E)$ and $\Delta G_\tau^s(\mathbf{r}, \mathbf{r}_1, E)$ [respectively the pseudovector and scalar contributions to the integral in Eq. (15)] when evaluated at $\mathbf{r}' = \mathbf{r}$ satisfy

$$\left[\Delta G_\tau^s\right]_{11} = \left[\Delta G_\tau^s\right]_{22} = \left[\Delta G_{-\tau}^s\right]_{11} = \text{even in } E, \qquad (21)$$

$$\left[\Delta G_\tau^v\right]_{11} = -\left[\Delta G_\tau^v\right]_{22} = -\left[\Delta G_{-\tau}^v\right]_{11} = \text{odd in } E. \qquad (22)$$

Taking into account the ordering of the basis in each valley, Eq. (13) yields corresponding deformation-induced shifts in

the local density of states that satisfy

$$\Delta\rho_{K,A}^s(\mathbf{r}, E) = -\Delta\rho_{K,A}^s(\mathbf{r}, -E) = \Delta\rho_{K',A}^s(\mathbf{r}, E)$$
$$= \Delta\rho_{K,B}^s(\mathbf{r}, E) = \Delta\rho_{K',B}^s(\mathbf{r}, E), \qquad (23)$$

$$\Delta\rho_{K,A}^v(\mathbf{r}, E) = \Delta\rho_{K,A}^v(\mathbf{r}, -E) = \Delta\rho_{K',A}^v(\mathbf{r}, E)$$
$$= -\Delta\rho_{K,B}^v(\mathbf{r}, E) = -\Delta\rho_{K',B}^v(\mathbf{r}, E). \qquad (24)$$

In summary, valleys K and K' contribute equally to the net change of LDOS $\Delta\rho_\ell(\mathbf{r}, E)$ experienced by each sublattice. While the contribution of the scalar potential to $\Delta\rho_\ell(\mathbf{r}, E)$ is identical for the two sublattices but odd in energy E, the shift coming from the vector potential is even in E but has opposite signs for $\ell = A$ and B. The last property will prove to be the origin of sublattice symmetry breaking in signatures of Kondo physics.

In the following sections, we present sublattice-resolved LDOS shifts $\Delta\rho_\ell^\alpha(\mathbf{r}, E)$ ($\alpha = v, s$) and the total LDOS $\rho_\ell(\mathbf{r}, E)$. The LDOS shifts are calculated via the method described above, numerically integrating Eq. (15) using the linearized approximation [Eq. (16)] for $\bar{G}_0(\mathbf{r}, \mathbf{r}', E)$. The full LDOS is computed as

$$\rho_\ell(\mathbf{r}, E) = \rho_0(E) + \sum_{\alpha=s,v} \Delta\rho_\ell^\alpha(\mathbf{r}, E), \qquad (25)$$

where $\rho_0(E)$ is the *exact* nearest-neighbor tight-binding density of states of pristine graphene [1]. The use of the exact $\rho_0(E)$ makes little difference on the energy scales $|E| \ll t_0$ spanned by Figs. 2 and 3 but it allows for a more realistic treatment of higher energy scales, important for an accurate computation of the Kondo temperature.

C. LDOS for graphene with a Gaussian bubble deformation

Figure 2 contains representative results for the graphene LDOS in the vicinity of a Gaussian bubble deformation. Data are shown at four different distances ($r = 0.5b$, $0.866b$, $1.3b$, and $1.8b$) from the center of the bubble along two different directions: $\phi = 90°$ (along a carbon-carbon bond direction, which forms the symmetry axis of one of the petals in the pseudomagnetic field) and $\phi = 75°$ (halfway in angle between the petal symmetry axis and a direction $\phi = 60°$ of zero pseudomagnetic field). The eight chosen locations are marked by white circles in Fig. 1(c). Along the direction $\phi = 90°$, $r = 0.866b$ is a position of maximum pseudomagnetic field B. At each r value, rotating from $\phi = 90°$ to $\phi = 75°$ moves off the petal symmetry axis, resulting in a reduction in B.

Figures 2(a)–2(d) show contributions to the change in the LDOS (valley summed, per spin orientation, per unit area) for sublattice A due to the vector ($\alpha = v$) and scalar ($\alpha = s$) gauge fields, plotted as $\Delta\rho_A^\alpha/(g_\alpha\eta^2)$ vs E/E_b, where $E_b = \hbar v_F/b$. Here, $g_\alpha\eta^2$ determines the maximum magnitude of the α field, while E_b is the natural energy scale associated with spatial variations over a length b. When scaled in this fashion, the LDOS changes at given r/b and ϕ are universal functions, independent of the deformation length scales (h_0 and b) as well as the gauge couplings (g_α). The results can be extended to negative values of E and to the B subattice using the symmetry relations in Eqs. (23) and (24).
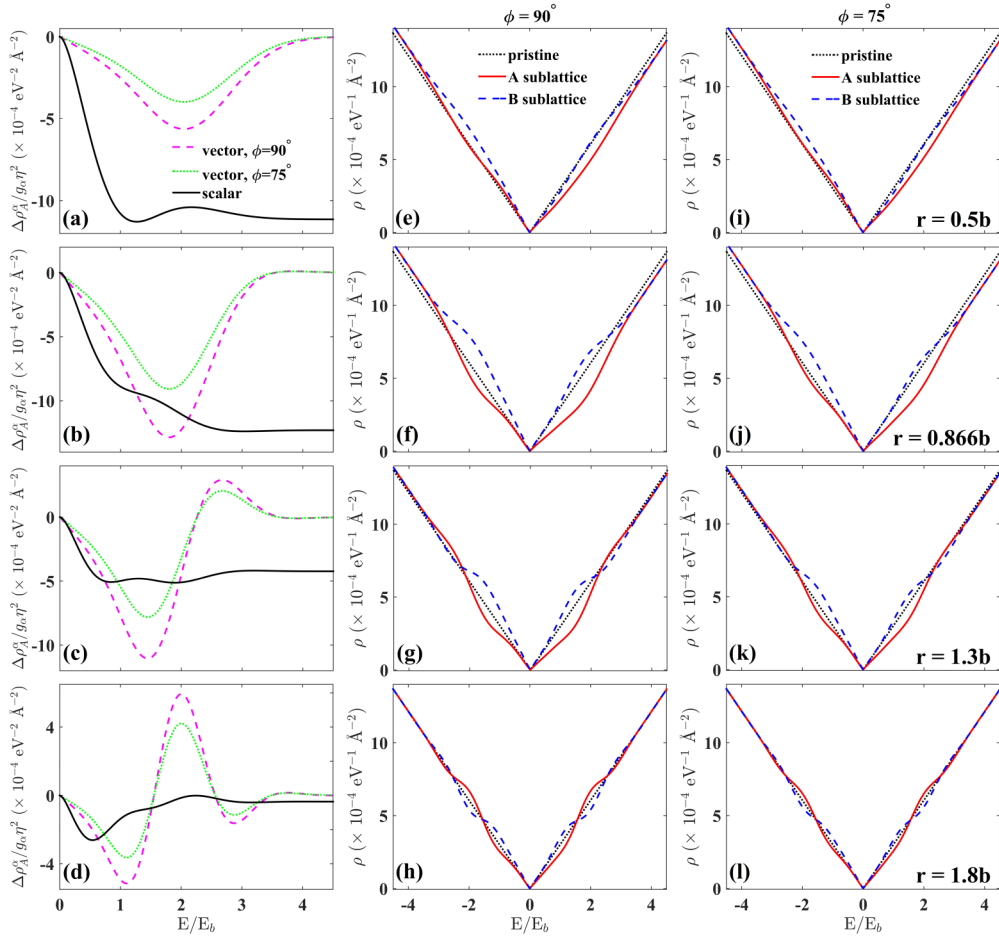
FIG. 2. LDOS near a Gaussian bubble. Each row shows data at a different radial distance r from the center of the deformation (labeled in the right panel) and at two polar angles $\phi = 90°$ and $75°$; see the locations marked by white dots in Fig. 1(c). (a)–(d) Scaled changes $\Delta\rho_A^\alpha/(g_\alpha\eta^2)$ in the A-sublattice LDOS (valley summed, per spin orientation, per unit area) due to the scalar ($\alpha = s$, solid lines) and vector ($\alpha = v$, dashed and dotted lines) gauge fields, plotted vs positive energy E divided by $E_b = \hbar v_F/b$. (Changes due to the scalar potential are independent of ϕ.) Note the different vertical scales in these panels. (e)–(h) LDOS (valley summed, per spin orientation, per unit area) for the A (solid lines) and B (dashed lines) sublattices at locations having coordinates $\phi = 90°$ and the radii r used in (a)–(d), respectively. The LDOS of pristine graphene is shown for reference (dotted lines). (i)–(l) Same as (e)–(h) except for locations at $\phi = 75°$. Data in (e)–(l) were calculated for $h_0 = 1$ nm, $b = 8$ nm, $g_v = 7$ eV, and $g_s = 3$ eV.

At each of the eight locations shown in Figs. 2(a)–2(d), the vector LDOS shift $|\Delta\rho_A^v(\mathbf{r}, E)|$ increases from zero at $E = 0$, passes through one or more maxima at energies $E \sim O(E_b)$, and then decreases toward zero for $E \gg E_b$. The oscillations on the energy scale E_b are the result of interference between scattering at different locations throughout the deformed region. The greatest value of $|\Delta\rho_A^v(\mathbf{r}, E)|$ over all E correlates closely with the magnitude of the pseudomagnetic field $B(\mathbf{r})$. The scalar shift $|\Delta\rho_A^s(\mathbf{r}, E)|$ rises from zero at $E = 0$, exhibits interference features around $E = O(E_b)$, and saturates for $E \gg E_b$ at a value proportional to $\Phi(\mathbf{r})$. This saturation behavior has a simple interpretation: for $E \gg E_b$, electrons experience an energy shift equal to the local scalar potential $\Phi(\mathbf{r})$, resulting in a LDOS shift $\Delta\rho_A^s(\mathbf{r}, E) = \rho_0[E - \Phi(\mathbf{r})] - \rho_0(E) \simeq -\Phi(\mathbf{r})/(2\pi\hbar^2v_F^2)$.

The functional form of the LDOS changes can be determined analytically for $|E| \ll E_b$. Due to the exponential decay of the scattering potentials $V_\tau(\mathbf{r}_1)$ and $\Phi(\mathbf{r}_1)$ for $|\mathbf{r}_1| \gg b$, the integral over $\mathbf{r}_1$ in Eq. (15) can be restricted to values of $|\mathbf{r}_1|$

smaller than a few times b. Then, the argument of the Hankel functions in Eq. (16), $kd \equiv (E/E_b)|\mathbf{r}_1 - \mathbf{r}|/b$, vanishes as $E/E_b \to 0$. Using the forms of the Hankel functions for small arguments, one can deduce that $\Delta\rho_A^v(\mathbf{r}, E) \propto |E/E_b|$ and $\Delta\rho_A^s(\mathbf{r}, E) \propto s_E(E/E_b)^2 \ln|E/E_b|$, relations that are in good agreement with our numerical data for $|E| \lesssim 0.1E_b$ for positions inside the deformed region. The corresponding analysis for positions outside this region results in a leading-order contribution from the vector potential proportional to $(E/E_b)^4 e^{-|E/E_b|^2}$ plus a term due to the scalar potential that behaves as $s_E(E/E_b)^2 \ln|E/E_b|$.

The remaining panels in Fig. 2 plot the full LDOS $\rho_A(\mathbf{r}, E)$ (solid line) and $\rho_B(\mathbf{r}, E)$ (dashed line) vs E/E_b for our reference case of a Gaussian bubble with a maximum height $h_0 = 1$ nm and a half-width $b = 8$ nm ($E_b \simeq 0.082$ eV), with couplings $g_v = 7$ eV and $g_s = 3$ eV. Figures 2(e)–2(h) show results for $\phi = 90°$ at the same r values as in Figs. 2(a)–2(d), respectively, while Figs. 2(i)–2(l) represent $\phi = 75°$. Each panel includes for comparison the linear LDOS of pristine
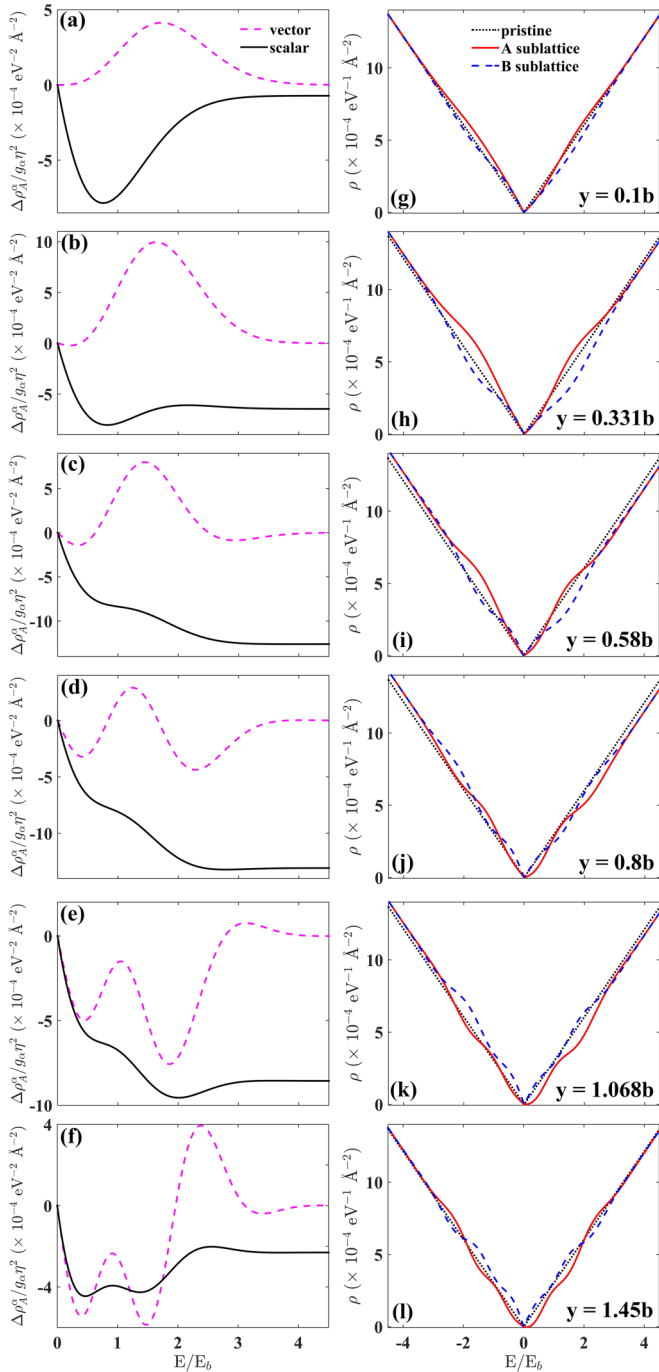
FIG. 3. LDOS near a long Gaussian fold. Each row shows data at a different perpendicular distance y from the central axis of the deformation (labeled in the right panel); see the locations marked by white dots in Fig. 1(c). (a)–(f) Scaled changes $\Delta\rho_A^\alpha/(g_\alpha\eta^2)$ in the A-sublattice LDOS (valley summed, per spin orientation, per unit area) due to the scalar ($\alpha = s$, solid lines) and vector ($\alpha = v$, dashed lines) gauge fields, plotted vs positive energy E divided by $E_b = \hbar v_F/b$. (g)–(l) LDOS (valley summed, per spin orientation, per unit area) for the A (solid lines) and B (dashed lines) sublattices at the locations considered in (a)–(f), respectively, calculated for $h_0 = 1$ nm, $b = 8$ nm, $g_v = 7$ eV, and $g_s = 3$ eV. The LDOS of pristine graphene is shown for reference (dotted lines).

graphene (dotted line). These plots clearly show the shift in spectral weight from $E > 0$ to $E < 0$ induced by the scalar potential Φ, as well as the spectral weight transfer between the two sublattices that arises from the pseudovector potential $\tau\mathbf{A}$. At each location $\mathbf{r}$, the greatest difference between the A and B sublattice LDOS occurs for energies $E \sim E_b$, while the greatest difference between the energy-integrated LDOS on the two sublattices occurs at the position $r = 0.866b$, $\phi = 90°$ of strongest pseudomagnetic field.

D. LDOS near a long Gaussian fold deformation

Figure 3 shows the LDOS (valley summed, per spin orientation, per unit area) near an extended Gaussian fold deformation. Results are presented for the six locations marked by white circles in Figs. 1(d) and 1(f), chosen to sample the range of coordinates y (measured from the fold axis $y = 0$) over which the pseudomagnetic field and the scalar deformation potential exhibit their strongest spatial variations. Figures 3(a)–3(f) plot changes in the A-sublattice LDOS due to the vector and scalar gauge fields, scaled in the same way as the results in the left column of Fig. 2. Just as for the bubble, $\Delta\rho_A^v/(g_v\eta^2)$ is largest at the locations of greatest magnitude of the pseudomagnetic field, which here are $y = 0.331b$ [Fig. 3(b)] and $y = 1.068b$ [Fig. 3(e)]. Similarly, $\Delta\rho_A^s/(g_s\eta^2)$ is largest at the peak location $y/b = 2^{-1/2} \simeq 0.7$ of the scalar potential [not far from the positions shown in Figs. 3(c) and 3(d)]. Larger y values are associated with increasing numbers of features in the $\Delta\rho_A^v(\mathbf{r}, E)$ around energy scales of order E_b, resulting from extended regions of interference as electrons scattering from the regions of largest pseudomagnetic field and scalar potential must travel longer path lengths en route to locations $\mathbf{r}$ further from the deformation axis.

Analysis of the low-energy asymptotic behavior of LDOS shifts is more complicated than in the case of the Gaussian bubble because (as noted above) the scattering region is unbounded along the x direction, allowing the arguments of the Hankel functions entering Eq. (16) to take arbitrarily large values for any $|E| \ll E_b$. For positions $|y| \gtrsim b$, both the vector and scalar LDOS shifts are well described for $|E| \lesssim 0.1E_b$ by a leading term proportional to $|E/E_b|$. The LDOS also exhibit oscillations at energies $E \gtrsim E_b$, similar to those shown by the bubble, that can be traced back to interference between scattering at different locations throughout the deformed region.

Figures 3(g)–3(l) plot the full LDOS $\rho_A(\mathbf{r}, E)$ (solid line) and $\rho_B(\mathbf{r}, E)$ (dashed line) vs E/E_b, for parameters $h_0 = 1$ nm, $b = 8$ nm ($E_b \simeq 0.082$ eV), $g_v = 7$ eV, and $g_s = 3$ eV. The LDOS for pristine graphene is included for reference (dotted lines). Particle-hole symmetry is broken due to the presence of the scalar potential, as seen most clearly in Figs. 3(i) and 3(j). The contribution from the vector potential to the LDOS change obtained through Eq. (15) is proportional to $\sin\phi_d$ and therefore involves destructive interference between scattering processes at every pair of locations symmetrically positioned at equal perpendicular distances from the fold axis. At $y = 0$, equal scattering strengths lead to perfect cancellation and $\Delta\rho_A^v(\mathbf{r}, E) = 0$ for all E. For other points inside the deformation region, however, such cancellation does not occur.

Crossings between $\Delta \rho_A(\mathbf{r}, E)$ and $\Delta \rho_B(\mathbf{r}, E)$ occur at energies where $\Delta \rho_\ell^v(\mathbf{r}, E)$ (which oscillates due to the interference processes mentioned above) passes through zero. For locations further from the symmetry axis of the fold [see, for example, Figs. 3(k) and 3(l)], some of the crossings are replaced by anticrossings.

III. KONDO PHYSICS

In this section, we consider a magnetic adatom on a distorted graphene membrane and find the effect of deformations on the characteristic Kondo screening temperature T_K. We focus on the most basic models for top- and hollow-site adsorption, disregarding additional complexities such as orbital degrees of freedom and coupling anisotropies [72] that have been shown to be important for certain adatoms. Our intention is to emphasize general Kondo signatures, independent of the nature of the adsorbate or the microscopic details of the hybridization. Section III A describes the Anderson impurity model used in our work and reviews certain properties of similar models for impurities in a conventional metallic host. Section III B applies the model to top-site adsorption on graphene, while Sec. III C addresses the hollow-site case.

A. Anderson impurity model

We investigate Kondo physics using a nondegenerate (single-orbital) Anderson impurity Hamiltonian for a magnetic adatom hybridized with a strained graphene host:

$$H = H_{\text{host}} + H_{\text{imp}} + H_{\text{hyb}}. \tag{26}$$

The host term is

$$H_{\text{host}} = \sum_{v,\sigma} \varepsilon_v \, c_{v,\sigma}^\dagger c_{v,\sigma}, \tag{27}$$

where $c_{v,\sigma}$ annihilates an electron in graphene with spin z projection $\sigma = \pm \frac{1}{2}$ (or, equivalently, $\uparrow / \downarrow$), nonspin quantum numbers that we collectively label v, and energy ε_v. The isolated adatom (or "impurity") is described by

$$H_{\text{imp}} = \varepsilon_d \sum_\sigma d_\sigma^\dagger d_\sigma + U \, d_\uparrow^\dagger d_\uparrow d_\downarrow^\dagger d_\downarrow, \tag{28}$$

where d_σ annihilates an electron of energy ε_d and spin σ in an orbitally nondegenerate level having an onsite Coulomb repulsion U. The coupling between the adatom and its host is captured in the term

$$H_{\text{hyb}} = \sum_{j,v,\sigma} W_j d_\sigma^\dagger \varphi_v(\mathbf{R}_j) c_{v,\sigma} + \text{H.c.}, \tag{29}$$

where W_j is the matrix element (assumed to be spin independent) for tunneling into the impurity level from the p_z orbital of carbon atom j at location $\mathbf{R}_j$ where the host eigenstate v has a (dimensionless) tight-binding wave function $\varphi_v(\mathbf{R}_j)$. The j sum runs over all carbon atoms in the graphene, even though W_j will be non-negligible only for a small number of carbons located close to the adatom. The wave function φ_v is defined only at the carbon sites, and is normalized so that

$$\langle \varphi_v | \varphi_{v'} \rangle = \sum_j \varphi_v^*(\mathbf{R}_j) \varphi_{v'}(\mathbf{R}_j) = \delta_{v,v'}. \tag{30}$$

In undeformed graphene, host eigenfunctions with small wave vectors $\mathbf{q} = (q \cos \phi_q, q \sin \phi_q)$ measured from the valley center at $\tau \mathbf{K}$ ($\tau = \pm 1$) and small energies $E = s_E \hbar v_F q$ ($s_E = \pm 1$) measured from the Dirac point can be written in the form

$$\varphi_{\ell, \tau, \mathbf{q}, s_E}(\mathbf{R}_j) = \frac{s_E^{\ell - 1}}{\sqrt{N_c}} e^{i(\tau \mathbf{K} + \mathbf{q}) \cdot \mathbf{R}_j} e^{i\tau(\ell - 3/2)\phi_q}, \tag{31}$$

where N_c is the number of unit cells in the graphene sheet, and $\ell = 1$ (A) or 2 (B) labels the sublattice to which carbon atom j belongs.

All single-particle energies (ε_v, ε_d, and the chemical potential μ) will be measured from the Dirac point in undistorted graphene. We will focus on situations where $\varepsilon_d - \mu < 0$ and $2(\varepsilon_d - \mu) + U > 0$ so that the ground state of the isolated impurity has a single electron that therefore forms a local magnetic moment.

Equation (29) can be rewritten as

$$H_{\text{hyb}} = \frac{1}{\sqrt{N_c}} \sum_{v,\sigma} \tilde{W}_v d_\sigma^\dagger c_{v,\sigma} + \text{H.c.}, \tag{32}$$

where

$$\tilde{W}_v = \sqrt{N_c} \sum_j W_j \, \varphi_v(\mathbf{R}_j). \tag{33}$$

It is convenient to transform to an energy representation by defining

$$a_{E,\sigma} = \sqrt{\frac{\pi}{N_c g(E)}} \sum_v \delta(E - \varepsilon_v) \tilde{W}_v c_{v,\sigma}, \tag{34}$$

with a (non-negative) hybridization function

$$g(E) = \frac{\pi}{N_c} \sum_v |\tilde{W}_v|^2 \, \delta(E - \varepsilon_v) \tag{35}$$

so that $\{a_{E,\sigma}, a_{E',\sigma'}^\dagger\} = \delta(E - E') \delta_{\sigma,\sigma'}$. This allows one to express Eq. (32) in the form

$$H_{\text{hyb}} = \sum_\sigma d_\sigma^\dagger \int dE \sqrt{g(E)/\pi} \, a_{E,\sigma} + \text{H.c.}, \tag{36}$$

and Eq. (27) in the form

$$H_{\text{host}} = \sum_\sigma \int dE \, E \, a_{E,\sigma}^\dagger a_{E,\sigma} + \cdots, \tag{37}$$

where "..." represents contributions from linear combinations of host states that do not couple to the impurity and that will not be considered any further.

Different possible symmetries of the impurity orbital and adsorption configurations on the surface of graphene can be modeled by appropriate choices of the matrix elements W_j entering Eq. (29). Both experiments and *ab initio* calculations suggest that two adsorption configurations are energetically most likely as follows [73]:

(1) "Top-site" attachment over a single carbon atom has been observed for Co adatoms on epitaxial monolayer graphene on SiC(0001), as well as for both Co and Ni on quasi-free-standing mononolayer graphene on SiC(0001) [74]. This configuration can be minimally described by just one nonzero W_j.

(2) "Hollow-site" attachment at the center of a carbon hexagon, as has been observed for Ni adatoms on monolayer graphene on SiC(0001) [74,75] and (in addition to top-site attachment) for both Co and Ni on quasi-free-standing monolayer graphene on SiC(0001) [74]. This case can be approximated by six nonzero values W_j, which may all be equal (e.g., for an s or d_{zz} impurity orbital) or may differ (as in the case of other d orbitals or any f orbital).

Anderson models for these two adsorption configurations on undistorted graphene have been considered previously; see, for example, Refs. [18,19,24,28,76,77]. In this paper we generalize these previous treatments to take into account deformation of the host surface.

Before discussing specific adsorption configurations, some general remarks are in order. Equations (26), (28), (36), and (37) together make up a standard representation of the Anderson impurity model for a magnetic impurity hybridizing with a host via an energy-dependent hybridization function $g(E)$. The canonical version of this model has chemical potential $\mu = 0$ and a "'top-hat" hybridization function

$$g(E) = \Gamma\,\Theta(D - |E|), \qquad (38)$$

where $\Theta(x)$ is the Heaviside function and the prefactor Γ is termed the "hybridization width." For any $\Gamma > 0$, the impurity spin degree of freedom becomes collectively screened by the conduction band at temperatures T below a crossover scale: the Kondo temperature T_K. The dependencies of physical properties on T, magnetic field B, and frequency ω are described by universal functions of T/T_K, B/T_K, and ω/T_K for $T, B, \omega \lesssim T_K$.[2] Provided that $U \ll D$, $\varepsilon_d - \mu \ll -\Gamma$, $U + \varepsilon_d - \mu \gg \Gamma$, and $2U\Gamma \ll \pi|\varepsilon_d - \mu|(U + \varepsilon_d - \mu)$ (conditions that place the model deep in its strongly correlated Kondo regime), the Kondo temperature can be written [78]

$$T_K \simeq 0.36\sqrt{\frac{2U g(\mu)}{\pi}}\exp\left[-\frac{\pi|\varepsilon_d - \mu|(U + \varepsilon_d - \mu)}{2U g(\mu)}\right], \quad (39)$$

where $\mu = 0$ and $g(\mu) = \Gamma$ in the canonical version of the model. In more general cases where $\mu \neq 0$ and/or $g(E)$ is not strictly constant, but still varies slowly within the energy range $|E - \mu| \lesssim U$ that sets T_K [78], the low-energy properties still follow the universal scaling forms with a Kondo scale given (up to an overall multiplicative correction) by Eq. (39).

Anderson models in which $g(E)$ has strong energy dependence near the chemical potential can exhibit strong deviations from canonical Kondo physics. A well-studied example is the pseudogap Anderson model [20–27], characterized by a hybridization function

$$g(E) = \Gamma\,|E/D|^r\,\Theta(D - |E|) \qquad (40)$$

with a band exponent $r > 0$. If the chemical potential μ is nonzero so that $g(\mu) > 0$, then the pseudogap Anderson model exhibits conventional physics for T, B, $|\omega| \lesssim T_K$, in many cases also retaining an exponential dependence of T_K on $g(\mu)$. For $\mu = 0$, by contrast, the depletion of hybridization close to the chemical potential allows Kondo screening of the impurity moment only if the hybridization width exceeds a

threshold value $\Gamma_c > 0$. For $\Gamma < \Gamma_c$, T_K effectively vanishes and the system instead approaches a low-energy regime in which the impurity moment asymptotically decouples from the conduction band. A quantum phase transition (QPT) at $\Gamma = \Gamma_c$ separates local-moment ($\Gamma < \Gamma_c$) and Kondo ($\Gamma > \Gamma_c$) phases. In each phase, physical properties take scaling forms that depend on the band exponent r entering Eq. (40) as well as T/T^*, B/T^*, and ω/T^*. Here, T^* (which replaces T_K in the conventional Anderson model) is a many-body scale that vanishes as $T^* \propto |\Gamma - \Gamma_c|^\nu$ close to the QPT, with ν being a positive, r-dependent exponent.

As pointed out previously [19,24,28,76,77], adsorption of a magnetic impurity in a top-site configuration on undeformed graphene can be described by an Anderson model with a hybridization function that at low energies $|E| \ll D = 3t_0$ corresponds to Eq. (40) with $r = 1$, while hollow-site adsorption realizes the case $r = 3$. This raises the prospect of realizing the pseudogap Kondo effect in undoped graphene where the chemical potential coincides with the Dirac points, but (as mentioned in Sec. I) there is a high likelihood that the characteristic scale T^* lies below the range accessible in experiments. Our focus in this work is on a different regime $|\mu| = O(E_b)$ that reveals unique features of Kondo physics in deformed graphene. Here, the low-energy properties follow their conventional (metallic) forms and the effects of strain can be captured in the variation of the Kondo temperature T_K for different adatom locations relative to the peak deformation.

To calculate T_K, we solve the appropriate Anderson impurity model using the numerical renormalization-group (NRG) method [79–82], as adapted to treat an arbitrary hybridization function [22]. The Kondo temperature is determined via the standard operational definition (with $g\mu_B = k_B = 1$) $T_K \chi_{\text{imp}}(T_K) = 0.0701$ [79,80], where $\chi_{\text{imp}}(T)$ is the impurity contribution to the system's magnetic susceptibility at absolute temperature T. All NRG results reported below were obtained using a Wilson discretization parameter $\Lambda = 2.5$, retaining up to $N_{\text{kept}} = 2000$ many-body spin multiplets after each iteration. A known artifact of NRG band discretization is a reduction in the hybridization width from its nominal value Γ to an effective one Γ/A [80]. When making comparisons with Eq. (39), we use the correction factor $A = 1.204$ [22] appropriate for $\Lambda = 2.5$ and a linear hybridization function [Eq. (40) with $r = 1$].

B. Top-site adsorption

When a magnetic atom adsorbs directly over a carbon atom, it is a good approximation to assume that there is just one non-negligible hybridization matrix element W. If the hybridizing carbon atom is at position **R** in sublattice ℓ, then the relevant Anderson impurity model has hybridization function

$$g_{\text{TS}}(E) = 2D\Gamma A_c \rho_\ell(\mathbf{R}, E), \qquad (41)$$

where $A_c = 3\sqrt{3}a^2/2$ is the graphene unit-cell area, $D = 3t_0$ is the half-bandwidth of graphene, $\Gamma = \pi W^2/(2D)$ is the mean value of $g_{\text{TS}}(E)$ taken over all $|E| < D$, and $\rho_\ell(\mathbf{R}, E)$ is the valley-summed local density of states per spin orientation, per unit area as discussed in Secs. II C and II D.

---

[2]We work in units where $\hbar = k_B = \mu_B = 1$.

Equation (41) shows that the hybridization function $g_{TS}(E)$ directly follows the energy dependence of the LDOS for the sublattice to which the hybridizing carbon belongs. In undeformed graphene, $\rho_\ell(\mathbf{R}, E)$ reduces for $|E| \ll D$ to $\rho_0(E)$ given in Eq. (17) and, thus, $g_{TS}(E) = (6\sqrt{3}/\pi)\Gamma|E/D|$. We assume that the slowly varying out-of-plane deformations considered in this study induce negligible change in the hybridization matrix element W, so that strains enter the Anderson model solely through changes in $\rho_\ell(\mathbf{R}, E)$.

In Secs. III B 1 and III B 2 below, we present results for mechanical deformations with the same geometric parameters as were used in Sec. II: maximum height $h_0 = 1$ nm, Gaussian half-width $b = 8$ nm (so that $E_b = \hbar v_F/b = 0.082$ eV), and gauge couplings $g_v = 7$ eV and $g_s = 3$ eV. In light of the disagreement in the literature over the sign and magnitude of g_s, we also show results for $g_s = -3$ and 1 eV. We consider situations where the graphene is gated or doped to produce a chemical potential $\mu = \pm 0.15$ eV $\simeq \pm 1.8E_b$ in the energy range of largest deformation-induced changes in the LDOS $\rho_\ell(\mathbf{R}, E)$ (see Secs. II C and II D).

It is also necessary to choose parameters ε_d, U, and Γ describing the adatom. To determine the parameter values appropriate for a particular magnetic impurity species would require *ab initio* calculations or detailed experimental measurements that are beyond the scope of this work. However, qualitative behaviors to be expected can be adequately illustrated by focusing on a single value of the level energy $\varepsilon_d = -1$ eV with either $U = -2\varepsilon_d = 2$ eV (for an impurity level that is particle-hole symmetric for $\mu = 0$) or $U = \infty$ (representing maximal particle-hole asymmetry). We choose 0.65 eV $\leqslant \Gamma \leqslant 3$ eV, values that cause the Kondo temperature T_K^0 in the absence of strain to fall between 20 mK and 4.2 K.

Let us start from the reference case of an adatom with parameters $U = -2\varepsilon_d = \Gamma = 2$ eV adsorbed on top of a carbon atom in undeformed graphene having a chemical potential $\mu = \pm 0.15$ eV. NRG calculations for this case give $T_K^0 = 0.21$ K, within 20% of the value 0.25 K predicted by Eq. (39). This close agreement suggests that, despite the complicated energy dependence of $g_{TS}(E)$, the Kondo scale is set mainly by the value of $g_{TS}(\mu)$. (We will return to this point when we discuss hollow-site adsorption.) That T_K^0 is independent of the sign of μ is due to the strict particle-hole symmetry about the Dirac points $\varepsilon = 0$ of the hybridization function [i.e., $g_{TS}(E) = g_{TS}(-E)$ for all E] and of the adatom energy levels (i.e., $U = -2\varepsilon_d$).

Having established this reference case, we can now look at the effects of deformation of the graphene host.

1. Kondo temperature for top-site adsorption near a Gaussian bubble

Figure 4 shows Kondo temperatures for an adatom on top of a carbon atom in sublattice A (data points connected by solid lines) or in sublattice B (dashed lines), located at four distances r from the peak of a Gaussian bubble along directions at $\phi = 90°$ (left panels) and $\phi = 75°$ (right panels) measured counterclockwise from the positive x axis. The locations illustrated are marked by white dots in Fig. 1(c) and correspond to the ones in Fig. 2. All data in this figure are for $U = -2\varepsilon_d = 2$ eV. Each row corresponds to a different
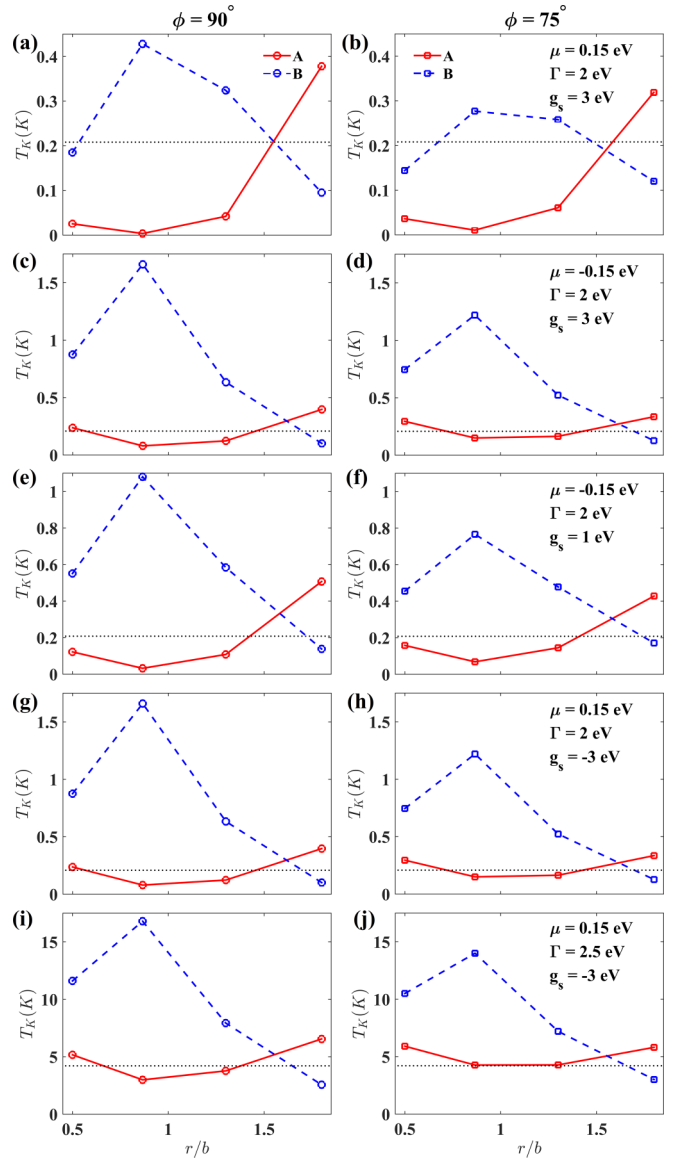

FIG. 4. Kondo temperature T_K vs distance r from the center of a Gaussian bubble deformation [Fig. 1(a)] along directions $\phi = 90°$ (left panels) and $\phi = 75°$ (right panels). Data are for height $h_0 = 1$ nm and width $b = 8$ nm, for gauge vector coupling $g_v = 7$ eV, and for a symmetric magnetic impurity described by $U = -2\varepsilon_d = 2$ eV. The other model parameters are specified in a legend for each row. Solid (dashed) lines connect T_K values for adatoms on top of carbon atoms in the A (B) sublattice. A horizontal dotted line represents the Kondo temperature in the absence of deformation.

combination of the chemical potential μ, the adatom hybridization width Γ, and the scalar gauge coupling g_s. Each row after the first differs from a higher row by a change in just one of μ, Γ, and g_s, chosen to illustrate and highlight a general trend as one moves within the parameter space of the model.

Figures 4(a) and 4(b) illustrate the case $g_s = 3$ eV for which the A- and B-sublattice LDOS are plotted in Fig. 2. The other parameters are $\mu = 0.15$ eV $\simeq 1.8E_b$ and $\Gamma = 2$ eV. At each of the eight locations illustrated, the scalar gauge potential decreases the LDOS on both sublattices, while the vector

gauge potential increases the LDOS on one sublattice and reduces it on the other sublattice, as expected from Eqs. (23) and (24); since the vector gauge coupling is larger than the scalar, the net effect at all locations except $(r, \phi) = (0.5b, 75°)$ is a net increase of $\rho_\ell(\mathbf{R}, \mu)$ for one sublattice and a net decrease for the other. Comparison between Figs. 2(e)–2(l), 4(a), and 4(b) reveals that T_K rises/falls in close correlation with the value of the sublattice LDOS at the chemical potential. The extremal T_K values occur at $r = 0.866b$, $\phi = 90°$, where the A sublattice has a density of states per unit area $\rho_A(\mu) = 0.0176/(DA_c)$ and a Kondo scale $T_K = 3.5$ mK, while the B sublattice has $\rho_B(\mu) = 0.0312/(DA_c)$ and $T_K = 0.43$ K; for comparison, pristine graphene has $\rho_0(\mu) = 0.0268/(DA_c)$ and (as noted above) Kondo temperature $T_K^0 = 0.21$ K. In this particular region near a bubble deformation, the LDOS at the chemical potential decreases by 34% on the A sublattice and increases by 16% on the B sublattice. These changes are amplified in the Kondo temperature, which (relative to undeformed graphene) decreases by a factor of 60 on the A sublattice while doubling on the B sublattice. However, the amplifications are not quite as strong as the 110-fold decrease for A and the 3.7-fold increase for B predicted by Eq. (39), reinforcing the point that T_K depends on values taken by the hybridization function $g_{TS}(E)$ within a window around the chemical potential, not just on $g_{TS}(\mu)$. Note in particular that, as can be seen in Fig. 2 and Eq. (41), a deformation that decreases (increases) $g_{TS}(\mu)$ tends to increase (decrease) $g_{TS}(E)$ at energies E not too far from μ. The subtle interplay of these changes in $g_{TS}(E)$ explains, for example, why deformation results in a modest decrease of T_K on the B sublattice at $r = 0.5b$, $\phi = 90°$ even though $\rho_B(\mathbf{r}, \mu)$ and hence $g_{TS}(\mu)$ undergo a slight increase.

Figures 4(c) and 4(d) illustrate the same situation as Figs. 4(a) and 4(b), respectively, apart from a reversal in sign of the chemical potential to $\mu = -0.15$ eV. As noted above, the Kondo temperature for our reference case in undeformed graphene is unchanged by this reversal due to the strict particle-hole symmetry of the LDOS and the adatom level energies. However, the scalar component of the LDOS changes induced by deformation breaks particle-hole symmetry; for $g_s > 0$, the effect is to decrease the LDOS for $E > 0$ and increase it for $E < 0$. Therefore, the case $\mu = -0.15$ eV samples a higher LDOS in the vicinity of the chemical potential than is the case for $\mu = 0.15$ eV, and as one might expect, higher Kondo temperatures follow. The highest and lowest Kondo temperatures in Figs. 4(c) and 4(d) are 1.7 K and 79 mK, respectively, 8 and 0.4 times T_K^0. That a modest (here 0.6%) strain can enhance T_K by an order of magnitude is one of the principal findings of this work. It significantly improves the prospects of experimental detection of Kondo physics in situations where the signatures would otherwise occur below the base temperature of an experiment.

Figures 4(e) and 4(f) differ from Figs. 4(c) and 4(d) only by a decrease in g_s from 3 to 1 eV, which reduces the magnitude of the particle-hole symmetry breaking caused by the scalar potential. The variation of T_K with position (r, ϕ) in Figs. 4(e) and 4(f) is qualitatively very similar to that in Figs. 4(c) and 4(d). However, each T_K in the third row of the figure is smaller than its counterpart in the second row, while still being greater than the corresponding value for $\mu = 0.15$ eV in the first row.

Figures 4(g) and 4(h) differ from Figs. 4(a) and 4(b) only by a switch in g_s from 3 to -3 eV, reversing the sign of the LDOS change due to the scalar potential while leaving unaffected the change due to the vector potential. For the cases considered here, where the undeformed $g_{TS}(E) = g_{TS}(-E)$ and $U = -2\varepsilon_d$, a change in sign of g_s while keeping μ constant has the same effect on T_K as a change in the sign of μ at fixed g_s. For this reason, the Kondo temperatures shown in Figs. 4(g) and 4(h) are identical to those in Figs. 4(c) and 4(d).

Finally, Figs. 4(i) and 4(j) differ from Figs. 4(g) and 4(h) only by an increase in Γ from 2 to 2.5 eV. This change increases the Kondo temperature T_K^0 for an undeformed host from 0.21 to 4.2 K. Near the Gaussian bubble, the pattern of T_K values on each sublattice is qualitatively very similar to that for $\Gamma = 2$ eV. However, Figs. 4(i) and 4(j) show values of T_K/T_K^0 spanning a range 0.61 to 4.0 that is narrower than the range 0.38 to 8.0 in Figs. 4(g) and 4(h). Such a reduction with increasing Γ in the sensitivity of the Kondo scale to deformation-induced LDOS changes is consistent with the approximation that T_K is given by Eqs. (39) and (41). For still greater values of the hybridization width, the system should cross over from its Kondo regime into mixed valence, where T_K depends linearly, rather than exponentially, on $g(\mu)$.

2. Kondo temperature for top-site adsorption near a long Gaussian fold

We now turn to Fig. 5, which shows Kondo temperatures for an adatom on top of a carbon atom in sublattice A (solid lines) or sublattice B (dashed lines) at six perpendicular distances y from the symmetry axis ($y = 0$) of an extended Gaussian fold. The locations illustrated are marked by white dots in Fig. 1(d) and are the ones for which the LDOS is plotted in Fig. 3. The left panel in each row shows data for the same combination of μ, g_s, $U = -2\varepsilon_d$, and Γ (and hence the same value of T_K^0) as appears in the corresponding row of Fig. 4, thereby facilitating the identification of similarities and differences between the effects of bubble and fold deformations. The right panel differs from its left counterpart only in that the data are for $U = \infty$ and Γ has been adjusted to keep T_K^0, the Kondo temperature in the absence of deformation, within the range 20 mK to 2–3 K. (Without any adjustment of Γ, the value of T_K^0 calculated for $U = \infty$ and our standard hybridization width $\Gamma = 2$ eV would be 24 μK for chemical potential $\mu = 0.15$ eV or 490 K for $\mu = -0.15$ eV, in both cases placing the Kondo scale outside the window of experimental interest for most experiments.)

Figures 5(a)–5(d) illustrate the case $g_s = 3$ eV for which the A- and B-sublattice LDOS are plotted in Fig. 3. Figures 5(a) and 5(b) are for $\mu = 0.15$ eV $\simeq 1.8E_b$, while Figs. 5(c) and 5(d) are for $\mu = -0.15$ eV. Comparison between these panels and Figs. 3(g)–3(l) reveals that (just as for the Gaussian bubble illustrated in Figs. 2 and 4), T_K varies within a panel in close correlation with the value of $\rho_\ell(\mathbf{R}, \mu)$. Due to a reversal in the sign of the vector gauge field compared to the bubble, for $|y| \lesssim 0.7b$ it is sublattice A (rather than B) that has the larger LDOS and hence the higher Kondo temperature. Nonetheless, the range of values of T_K/T_K^0 for $U = -2\varepsilon_d$ shown in Figs. 5(a) and 5(c) is similar to that for
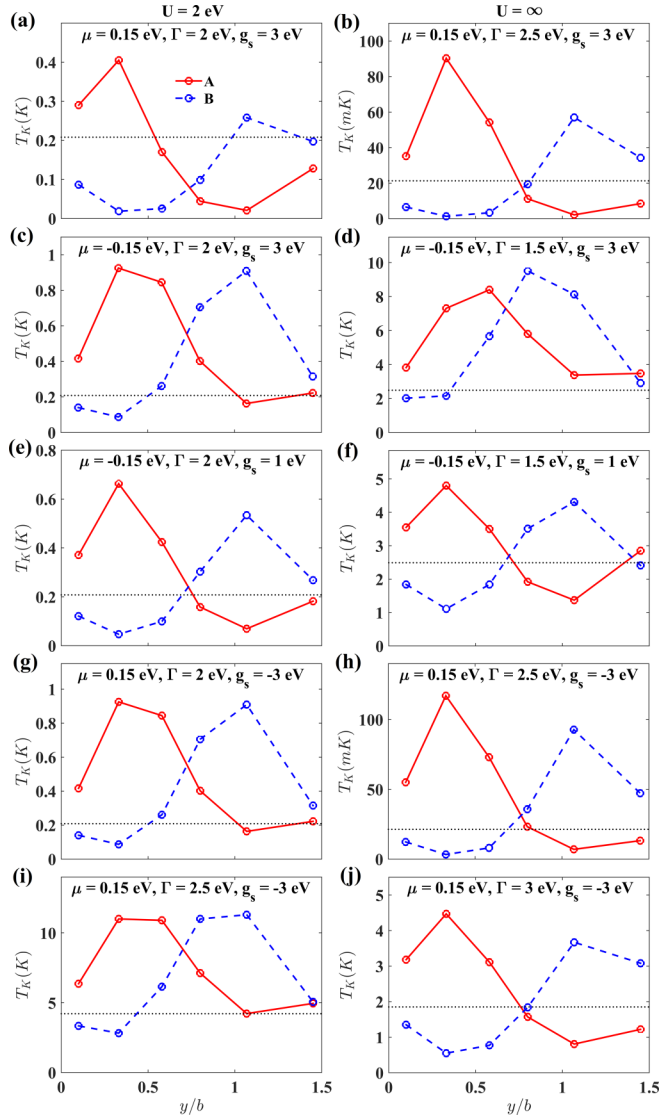
FIG. 5. Kondo temperature T_K vs distance y away from the symmetry axis of an extended Gaussian fold deformation [Fig. 1(b)]. Data are for height $h_0 = 1$ nm and width $b = 8$ nm, for gauge vector coupling $g_v = 7$ eV, for an impurity level energy $\varepsilon_d = -1$ eV, and for onsite Coulomb interactions $U = 2$ eV (left panels) and $U = \infty$ (right panels). All other model parameters are specified in a legend for each row. Those for the left panels are identical to the ones in the corresponding row of Fig. 4. Each panel in the right column shares the same μ and g_s as its left neighbor, but has a different Γ. Solid (dashed) lines connect T_K values for adatoms on top of carbon atoms in the A (B) sublattice, and a horizontal dotted line represents the Kondo temperature in the absence of deformation.

the bubble in Figs. 4(a)–4(d). For $U = \infty$, there is a much stronger difference between the behavior for $\mu = 0.15$ eV and -0.15 eV: in the former case, even with Γ increased to 2.5 eV the Kondo temperature on undeformed graphene is only $T_K^0 = 21$ mK, an order of magnitude smaller than in our reference case $U = -2\varepsilon_d = \Gamma = 2$ eV; for $\mu = -0.15$ eV, by contrast, even with Γ reduced to 1.5 eV, we find an order-of-magnitude enhancement of T_K^0 to 2.5 K.

The asymmetric behavior seen for $U = \infty$ under reflection of the chemical potential about the Dirac point can be understood within a poor man's scaling analysis of the Anderson model [16,83] that progressively integrates out the conduction-band states lying furthest in energy from the chemical potential, accounting for the eliminated band-edge states through perturbative adjustment of ε_d, U, and $g(E)$. For $U = \infty$, the renormalized value of the level energy $\tilde{\varepsilon}_d$ evolves according to the differential equation [83]

$$\pi \frac{d\tilde{\varepsilon}_d}{d\tilde{D}} = \frac{\tilde{\Gamma}(\tilde{D} + \mu)}{\tilde{D} - (\tilde{\varepsilon}_d - \mu)} - \frac{2\tilde{\Gamma}(-\tilde{D} + \mu)}{\tilde{D} + (\tilde{\varepsilon}_d - \mu)}, \quad (42)$$

where $\tilde{D}$ (with initial value $D + |\mu|$ and satisfying $d\tilde{D} < 0$) is the running half-bandwidth as measured from the chemical potential and $\tilde{\Gamma}(\pm \tilde{D} + \mu)$ represents the renormalized hybridization function evaluated at the edges of the reduced band. The factor of 2 in the second term on the right-hand side of Eq. (42) arises because an electron of either spin z projection $s = \pm \frac{1}{2}$ can undergo virtual tunneling from the bottom of the band into the empty impurity level. Virtual tunneling of the electron from a singly occupied impurity level to the upper band edge (described by the first term on the right side) has no factor of 2 because it must conserve the spin of that electron. Equation (42) shows that band states below, but not very far from, the chemical potential make a greater contribution to the renormalization of $\tilde{\varepsilon}_d$ than do band states an equal distance above the chemical potential. Due to the presence of the Dirac point at $E = 0$, the LDOS at energy $E = \mu - \tilde{D}$ for a given $\tilde{D} > 0$ is lower for $\mu = 0.15$ eV than it is for $\mu = -0.15$ eV. A faster scaling of $\tilde{\varepsilon}_d$ with decreasing $\tilde{D}$ generally results in a higher Kondo temperature [83], so it is to be expected that T_K^0 is higher for $\mu < 0$.

Figures 5(e) and 5(f) differ from Figs. 5(c) and 5(d) only by a decrease in g_s from 3 to 1 eV, which reduces the particle-hole symmetry breaking caused by the scalar potential. As was the case for Fig. 4, the variation of T_K with position in Figs. 5(e) and 5(f) is qualitatively similar to that in Figs. 5(a)–5(d), but at a given location, T_K for each sublattice lies between the corresponding values in the first and second rows of the figure.

Figure 5(g) differs from Fig. 5(a) only by a switch in the sign of g_s. As discussed in connection with Figs. 4(g) and 4(h), for $U = -2\varepsilon_d$ this switch is equivalent to changing the sign of μ, implying that the data in Fig. 5(g) are identical to those in Fig. 5(c). By contrast, there is no simple relation between the T_K values in Figs. 5(a) and 5(h), which differ not only as to the sign of g_s, but also in their values of Γ. Even if the Γ values were the same, there would be no symmetry connecting these two $U = \infty$ cases.

Finally, in Figs. 5(i) and 5(j) differ from Figs. 5(g) and 5(h), respectively, only by an increase in Γ by 0.5 eV. This change increases the Kondo temperature for an undeformed host from $T_K^0 = 0.21$ K in Fig. 5(g) to $T_K^0 = 4.2$ K in Fig. 5(i), and from $T_K^0 = 21$ mK in Fig. 5(j) to $T_K^0 = 1.9$ K in Fig. 5(j). The pattern of T_K values on each sublattice is qualitatively very similar for the smaller and larger Γ values, but (just as is seen for the bubble), the larger Γ yields ratios T_K/T_K^0 that deviate less from 1, indicating that as the system moves from deep in its Kondo regime toward mixed valence, the Kondo

temperature becomes less sensitive to deformation-induced changes in the LDOS on each sublattice.

To summarize, Figs. 4 and 5 show many similarities between the spatial variation of T_K for top-site adsorption near a Gaussian deformation of bubble and fold geometry. The most striking feature is that the Kondo temperature, a quantity that can be deduced from scanning-tunneling spectroscopy performed over adatom, serves to amplify deformation-induced changes in the LDOS. The degree of enhancement or suppression of T_K relative to its value T_K^0 for undeformed graphene depends on properties of the adatom (as modeled via the parameters ε_d, U, and Γ), on characteristics of the graphene (such as the parameters g_s and g_v and the degree of strain), and on environmental details such as the chemical potential μ established via doping or back gating. However, without any fine tuning of parameters, we have demonstrated that T_K can easily be enhanced by an order of magnitude, increasing the prospects for experimental observation of Kondo phenomenology.

In the top-site configuration, the effective scalar potential Φ defined in Eq. (6) tends to modify the Kondo temperature on both sublattices in the same direction, lowering T_K in situations where the chemical potential has the same sign as g_s but raising it when μ and g_s have the opposite sign. By contrast, the vector potential defined in Eq. (5) changes T_K in the opposite direction for adatoms attached to the A and B sublattices, but the direction of change for a given sublattice is unaffected by reversal in the sign of μ. These differing trends provide a signature that can unambiguously distinguish Kondo physics from other phenomena that may occur in graphene.

On a more speculative level, the results in Figs. 4 and 5 also suggest a possible method for disentangling the scalar and vector contributions to the deformation-induced LDOS change. Suppose that for a given adatom species and a fixed chemical potential μ, it is possible to measure (e.g., via the width of an STM Fano line shape) not only the Kondo temperature T_K^0 for top-site adsorption on pristine graphene, but also the scales $T_K^A(\mathbf{R})$ and $T_K^B(\mathbf{R})$ for adsorption above close-lying A- and B-sublattice carbon atoms in the vicinity of a smooth deformation. As noted above, and further discussed below in connection with Fig. 7, Eq. (39) proves to be reasonably accurate for top-site adsorption deep in the Kondo regime. Using Eq. (41), and decomposing the LDOS in the presence of deformation according to Eq. (25), one can estimate the fractional LDOS change due to the scalar effective potential,

$$\Delta\rho_A^s(\mathbf{R})/\rho_0(\mu) \simeq c \, \ln\left[T_K^A(\mathbf{R})T_K^B(\mathbf{R})/\left(T_K^0\right)^2\right], \quad (43)$$

as well as its counterpart due to the vector effective potential,

$$\Delta\rho_A^v(\mathbf{R}, \mu)/\rho_0(\mu) \simeq c \, \ln\left[T_K^A(\mathbf{R})/T_K^B(\mathbf{R})\right], \quad (44)$$

where c is a dimensionless constant that is independent of $\mathbf{R}$. By applying Eqs. (43) and (44) at different points $\mathbf{R}$ relative to the peak deformation, one should be able to gain insight into the sign and magnitude of the coupling g_s relative to the better-understood quantity g_v.

Even though we have considered a relatively small number of combinations of model parameters, the results in Figs. 4
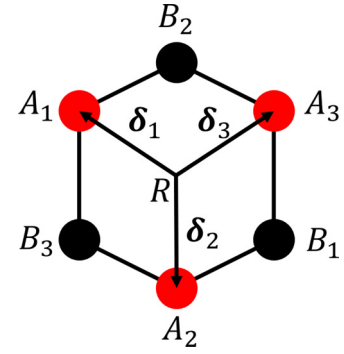

FIG. 6. Schematics of the hollow-site geometry. The impurity adatom, located directly above the point labeled R, hybridizes with the six nearest carbon atoms in the plane represented as circles. Nearest carbon atoms A_j ($j = 1, 2, 3$) from sublattice A (red circles) are located at positions described by two-dimensional vectors $\boldsymbol{\delta}_j$, while nearest carbon atoms B_j from sublattice B (black circles) are located at $-\boldsymbol{\delta}_j$.

and 5 are broadly representative of the range of qualitative behaviors that can be expected across the full parameter space. Additional complexities, such as adatoms having higher spins or spin-anisotropic interactions, are likely to alter only in quantitative detail the Kondo amplification of deformation-induced LDOS changes that is the central result of this work.

C. Hollow-site adsorption

The description of hollow-site adsorption is more complicated than that of the top-site configuration due to quantum-mechanical interference between tunneling from the active impurity level to different carbon atoms in monolayer graphene. We first treat adsorption at a hollow site on pristine graphene before considering the effects of deformation.

1. Hollow-site adsorption on pristine graphene

For simplicity, we assume that the adatom is located above point $\mathbf{R}$ on the graphene plane and hybridizes only with the six nearest carbon atoms (see Fig. 6): three from sublattice A at locations $\mathbf{R}_{A,n} = \mathbf{R} + \boldsymbol{\delta}_n$ ($n = 1, 2, 3$) and three from sublattice B at locations $\mathbf{R}_{B,n} = \mathbf{R} - \boldsymbol{\delta}_n$, with $\boldsymbol{\delta}_1 = (-\sqrt{3}, 1)a/2$, $\boldsymbol{\delta}_2 = (0, -1)a$, and $\boldsymbol{\delta}_3 = (\sqrt{3}, 1)a/2$. In general, the hybridization matrix elements W_j between the active impurity orbital and the nearest carbon atoms can take independent values $W_{A,n}$ and $W_{B,n}$. In previous studies [19,24,76,77], the hybridization function $g_{HS}(E)$ for hollow-site adsorption was calculated by substituting into Eq. (35) the expression

$$\tilde{W}_\nu = \sum_{n=1}^{3}[W_{A,n}\varphi_{A,\nu}(\mathbf{R}_{A,n}) + W_{B,n}\varphi_{B,\nu}(\mathbf{R}_{B,n})] \quad (45)$$

with $\nu = (\tau, \mathbf{q}, s_E)$ and $\varphi_{\ell,\tau,\mathbf{q},s_E}(\mathbf{r})$ being a plane-wave state defined in Eq. (31).

Reference [19] identifies two different classes of hollow-site adsorption. In situations where

$$W_{A,n} = W_A \quad \text{and} \quad W_{B,n} = W_B \quad \text{for } n = 1, 2, 3, \quad (46)$$

such that the adatom hybridizes equally with the three nearest carbons on a given sublattice, $g_{HS}(E) \propto |E/D|^3$ at low energies. In all other cases, where the set of hybridization matrix elements breaks the full C_{3v} point-group symmetry of the lattice, one instead finds $g_{HS}(E) \propto |E/D|$, qualitatively the same as for top-site adsorption. The additional factor of $(E/D)^2$ in the first class can be attributed to the appearance in $|\tilde{W}_{\tau,\mathbf{q},s_E}|^2$ of a multiplicative factor of $|\sum_{n=1}^{3} \exp[i(\tau \mathbf{K} + \mathbf{q}) \cdot \delta_n]|^2$, which vanishes at the valley minimum $\mathbf{q} = 0$.

Anticipating extension of the calculation to situations with deformation, we can instead derive the hybridization function $g_{HS}(E)$ from the continuum-limit single-particle Green's function in the basis (ψ_A, ψ_B):

$$
\begin{aligned}
G(\mathbf{r}, \mathbf{r}', E) &= \sum_{\nu,\nu'} \langle \mathbf{r} | \nu \rangle \langle \nu | (E + is_E \, 0^+ - H)^{-1} | \nu' \rangle \langle \nu' | \mathbf{r}' \rangle \\
&= \sum_{\nu} \frac{1}{E + is_E 0^+ - \varepsilon_\nu} \\
&\quad \times \begin{pmatrix} \psi_{A,\nu}(\mathbf{r}) \psi_{A,\nu}^*(\mathbf{r}') & \psi_{A,\nu}(\mathbf{r}) \psi_{B,\nu}^*(\mathbf{r}') \\ \psi_{B,\nu}(\mathbf{r}) \psi_{A,\nu}^*(\mathbf{r}') & \psi_{B,\nu}(\mathbf{r}) \psi_{B,\nu}^*(\mathbf{r}') \end{pmatrix}. \quad (47)
\end{aligned}
$$

The continuum-limit wave functions $\psi_{\ell,\nu}(\mathbf{r})$ are defined at all two-dimensional position vectors $\mathbf{r}$ within the graphene sheet of total area A, and are normalized so that

$$
\langle \psi_{\ell,\nu} | \psi_{\ell,\nu'} \rangle = \int d^2 \mathbf{r} \, \psi_\nu^*(\mathbf{r}) \, \psi_{\nu'}(\mathbf{r}) = \delta_{\nu,\nu'}. \quad (48)
$$

These continuum-limit wave functions can be connected with the tight-binding ones entering Eq. (33) via $\psi_{\ell,\nu}(\mathbf{r}) = A_c^{-1/2} \varphi_{\ell,\nu}(\mathbf{r})$, where A_c is the area of the graphene unit cell. This allows one to write

$$
g_{HS}(E) = -s_E A_c \, \text{Im} \sum_{n,n',\ell,\ell'} W_{\ell,n} W_{\ell',n'}^* [G(\mathbf{R}_{\ell,n}, \mathbf{R}_{\ell',n'}, E)]_{\ell\ell'}. \quad (49)
$$

In the range $|E| \ll t_0$, one can reduce the above to a sum over contributions from valley-resolved Green's functions $G_\tau(\mathbf{r}, \mathbf{r}', E)$ defined in Eq. (14).

Equation (49) can be evaluated in closed form within the approximation of linear dispersion about the Dirac points. Here, we illustrate this by summarizing the results for configurations with full C_{3v} symmetry [i.e., satisfying Eq. (46)] where, moreover, W_A/W_B is real. This encompasses as special cases both (a) $W_A = W_B$ describing an active impurity orbital that has cylindrical symmetry about an axis perpendicular to the graphene plane, as is the case for s, d_{zz}, and f_{z^3} orbitals, and (b) $W_A = -W_B$, appropriate for $f_{x(x^2-3y^2)}$ and $f_{y(y^2-3x^2)}$ orbitals. After some laborious algebra, one finds that the $\ell \neq \ell'$ terms in Eq. (49) sum to zero, while the $\ell = \ell'$ terms combine to give

$$
g_{HS}(E) = \frac{36\sqrt{3}}{\pi} \Gamma |E/D| [1 - J_0(2\sqrt{3}|E|/D)] \quad (50)
$$

with $\Gamma = \pi(|W_A|^2 + |W_B|^2)/(4D)$. On the right-hand side of Eq. (50), the term 1 inside the square brackets comes from pure LDOS ($n = n'$) terms in Eq. (49), while the zeroth-order Bessel function comes from nonlocal ($n \neq n'$) terms. In the regime where $2\sqrt{3}|E|/D \ll 1$, the approximation $J_0(x) \simeq 1 - x^2/4$ leads to $g_{HS}(E) \simeq (108\sqrt{3}/\pi)\Gamma|E/D|^3$, consistent

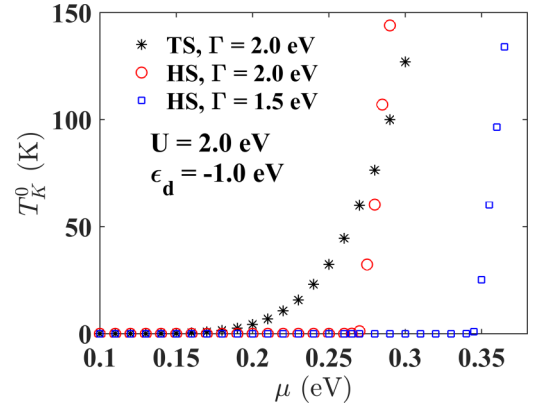FIG. 7. Kondo temperature T_K^0 vs chemical potential μ for an adatom with $U = -2\varepsilon_d = 2$ eV on pristine (undeformed) graphene, showing data for top-site adsorption with hybridization width $\Gamma = 2$ eV ($*$) as well as C_{3v}-symmetric hollow-site adsorption with $\Gamma = 2$ eV (open circle) and $\Gamma = 1.5$ eV (open square).

with previous work [19,24,76,77]. The additional factor of $(E/D)^2$ compared with $g_{TS}(E) \propto |E/D|$ arises from the complete destructive interference at the Dirac points ($E = 0$) between (i) virtual tunneling of an electron from a given carbon atom in sublattice ℓ into the active impurity level, then from the impurity back to the same carbon atom, and (ii) similar processes that end with the electron tunneling back to one of the other two nearest carbons belonging to sublattice ℓ.

The cubic energy dependence of $g_{HS}(E)$ for small $|E/D|$ means that hybridization is greatly suppressed for hollow-site adsorption compared with its top-site counterpart. Hence, for a chemical potential close to the Dirac point and any given combination of the parameters ε_d, U, and Γ, the Kondo scale T_K^0 will generally be much lower in the hollow-site configuration, as noted previously in Ref. [28]. We illustrate this tendency in Fig. 7, which plots the Kondo temperature T_K^0 vs the chemical potential μ for three different cases, all involving a magnetic impurity level with $U = -2\varepsilon_d = 2$ eV. Asterisks show T_K^0 for top-site adsorption of an impurity having hybridization width $\Gamma = \pi W^2/(2D) = 0.2$ eV. Over the range of μ spanned in the figure, the numerical data agree with Eq. (39) to within better than a factor of 4. This observation supports the assessment made near the start of Sec. III B that the Kondo physics for top-site adsorption on graphene is essentially conventional, with the effect of the pseudogap in the density of states being adequately captured through the value of $g_{TS}(\mu)$.

The remaining points in Fig. 7 represent T_K^0 for C_{3v}-symmetric hollow-site adsorption, calculated assuming that $g_{HS}(E) = 6[1 - J_0(2\sqrt{3}|E|/D)] g_{TS}(E)$, a relation that holds rigorously only for the region $|E| \ll D$ of linear dispersion. Although there are doubtless some corrections to this relation within the energy range $|E - \mu| \lesssim U$ that determines T_K [78], the approximation is adequate to illustrate the qualitative differences between top- and hollow-site adsorption. The circles in Fig. 7 correspond to the same hybridization width $\Gamma = 2$ eV illustrated for top-site adsorption, and show that T_K^0 is so small for $\mu \lesssim 0.26$ eV as to be completely inaccessible to experiments, but then rises rapidly over a narrow range of

chemical potential so that for $\mu \gtrsim 0.28$ eV, it exceeds the Kondo scale for top-site adsorption. Over the entire range of μ covered in the figure, the hollow site T_K^0 exceeds by at least 50 orders of magnitude the value predicted by Eq. (39), pointing to strong departures from conventional Kondo physics.

Based on the spatial geometries, we believe it likely that for a given adatom, hollow-site adsorption will involve a smaller wave-function overlap between the active impurity level and the p_z orbital on any of the nearest carbon atoms than would be the case for top-site adsorption. This suggests that the top-site case $\Gamma = 2$ eV should more properly be compared with hollow-site adsorption for some value $\Gamma < 2$ eV. The first-principles calculations required to estimate the appropriate value of Γ are beyond the scope of this work. However, the general idea can be seen by considering sample data for $\Gamma = 1.5$ eV, plotted with squares in Fig. 7. The T_K^0 vs μ curve for this case has the same shape as its hollow-site counterpart for $\Gamma = 2$ eV, but it is shifted to higher μ values. Not surprisingly, further reductions in Γ lead to even larger shifts in the curve.

If the hybridization matrix elements do not satisfy Eq. (46), as will be the case for most d and f atomic orbitals, then following the arguments in Ref. [19], one should expect $\Gamma_{\text{HS}}(E)$ for undeformed graphene instead to vanish linearly for $|E| \ll D$, with a prefactor that depends on the degree of C_{3v} symmetry breaking. In such cases, the dependence of the Kondo scale on chemical potential should be very similar to that shown in Fig. 7 for top-site adsorption, quite possibly with a shift to the right arising from reduced hybridization matrix elements.

Results such as those shown in Fig. 7 suggest that experimental observation of the Kondo effect for adatoms on undeformed graphene will depend on the ability, via doping or application of back-gate voltages, to move the chemical potential significantly (e.g., several hundred meV) away from the Dirac point. Top-site and C_{3v}-symmetry-breaking hollow-site adsorption are expected to display an exponential dependence of the Kondo temperature on the value of the host LDOS at the chemical potential. Due to tunneling interference effects, C_{3v}-symmetric hollow-site adsorption should exhibit an even greater sensitivity to the location of the chemical potential.

2. Hollow-site adsorption on deformed graphene

Equation (49) remains valid in the presence of smooth out-of-plane deformations of the graphene monolayer. As discussed in Secs. II A and II B, such deformations modify the continuum-limit electronic Green's function $G(\mathbf{r}, \mathbf{r}', E)$. Nearby deformations are likely also to modify the hybridization matrix elements W_j between a hollow-site adatom and its surrounding carbon atoms. In general, both the changes in the Green's function and those in the hybridization matrix elements will break any C_{3v} symmetry about the impurity site that might have been present when the graphene was undistorted, and can be expected to introduce into $g_{\text{HS}}(E)$ terms proportional to η^2 (the strain measure introduced in Sec. II A) that vanish at the Dirac points as $|E/D|$. Terms arising from changes in the Green's function should reach their greatest magnitude at energies $|E| = O(E_b)$, as is the case for top-site adsorption, while terms originating in changes in the

hybridization matrix elements likely extend throughout the energy range $|E| \lesssim D/6$ of Dirac dispersion. Since a hollow-site adatom couples to both sublattices, deformations will have an overall more muted impact on the Kondo temperatures than for top-site adsorption and will not lead to distinctive alternating patterns analogous to the ones described Sec. III B.

As shown in Sec. III C 1, the Kondo scale for C_{3v}-symmetric hollow-site adsorption in pristine graphene varies almost as a step function with respect to variation of the chemical potential, rising over a very narrow window of μ from being undetectably small to become larger than T_K^0 for top-site adsorption. Unless an experimental system is fine tuned into this window, the deformation-induced effects discussed in the preceding paragraph will have negligible effect on the Kondo temperature and on the prospects for experimental observation of Kondo physics. For this reason, little purpose is served by performing detailed numerical calculations for hollow-site adsorption in the presence of deformation.

IV. DISCUSSION

The theoretical and numerical work reported in this paper has investigated factors that influence the characteristic temperature T_K and energy scale $k_B T_K$ of the Kondo effect for adatoms on graphene. The two-dimensional host enters the Kondo physics through the hybridization function $g(E)$, which provides a spectral description of adatom-host orbital overlaps. Depending on the adsorption geometry, $g(E)$ for pristine graphene is expected to vanish with an either linear or cubic dependence on $|E|$ on approach to the Dirac points at $E = 0$. As a result, T_K shows strong sensitivity to the position of the chemical potential μ. For top-site adsorption of the magnetic atom directly above a single host carbon, T_K displays an exponential dependence on μ that is captured quite well by substituting the value $g(\mu) \propto |\mu|$ into the standard expression for the Kondo scale in a conventional metal. Adsorption of the magnetic atom in the hollow site in a high-symmetry configuration at the center of a carbon hexagon, described by $g(E) \propto |E|^3$ for $|E|$ much smaller than the half-bandwidth, yields a much sharper, almost steplike variation of T_K with increasing μ. As a result, prospects of probing the Kondo regime $T \lesssim T_K$ for hollow-site adsorption hinge on the ability to dope or gate the chemical potential far from the Dirac points.

The main focus of the paper has been the exploration of strain as a tool for enhancing the value of T_K and revealing unique aspects of the Kondo effect in graphene. We have shown that different placements of magnetic adatoms relative to the peak of a slowly varying deformation yield wide variations in the Kondo screening temperature with a spatial dependence that amplifies an underlying pattern of strain-induced changes in the local density of states. Fairly modest (smaller than 1%) strains can locally increase the Kondo temperature for a top-site adatom coupled to a single carbon atom from one sublattice by at least an order of magnitude compared to the situation in undeformed graphene, while simultaneously decreasing by a similar factor T_K for nearby adsorption to the other sublattice. These effects can be observed over a wide range of the model parameters ε_d, U, and Γ describing

the adatom and its hybridization with the graphene host, and depend crucially only on the chemical potential lying in the general energy range where the LDOS on each sublattice is significantly affected by the deformation. This unique pattern of spatial variation can be used as a fingerprint to identify the Kondo regime for adatoms on graphene. Magnetic adatoms attached in other geometries, such as the hollow-site configurations, are expected to experience weaker strain-induced modulations in T_K.

In recent years, much progress has been achieved in the area of substrate engineering for graphene [8,62]. Setups like those reported in Ref. [62], for example, create a periodic strain modulation in graphene deposited on top of SiO_2 nanospheres. The weak graphene-substrate hybridization in such experiments makes applicable the theoretical description developed in this paper. Local probes, combined with atomic manipulation of adatom placement, should allow observation of variations in T_K that map strain fields at a truly microscopic level.

[1] A. H. Castro Neto, F. Guinea, N. M. R. Peres, K. S. Novoselov, and A. K. Geim, Rev. Mod. Phys. **81**, 109 (2009).

[2] M. I. Katsnelson, *Graphene: Carbon in Two Dimensions* (Cambridge University Press, Cambridge, 2012).

[3] W. Chen, X. Gui, B. Liang, M. Liu, Z. Lin, Y. Zhu, and Z. Tang, ACS Appl. Mater. Interfaces **8**, 10977 (2016).

[4] S. Deng and V. Berry, Mater. Today **19**, 197 (2016).

[5] L. Yang, T. Niu, H. Zhang, W. Xu, M. Zou, L. Xu, G. Cao, and A. Cao, 2D Mater. **4**, 041001 (2017).

[6] K. Kim, Z. Lee, B. D. Malone, K. T. Chan, B. Alemán, W. Regan, W. Gannett, M. F. Crommie, M. L. Cohen, and A. Zettl, Phys. Rev. B **83**, 245433 (2011).

[7] H. Lim, J. Jung, R. S. Ruoff, and Y. Kim, Nat. Commun. **6**, 8601 (2015).

[8] Y. Jiang, J. Mao, J. Duan, X. Lai, K. Watanabe, T. Taniguchi, and E. Y. Andrei, Nano Lett. **17**, 2839 (2017).

[9] J. Zabel, R. R. Nair, A. Ott, T. Georgiou, A. K. Geim, K. S. Novoselov, and C. Casiraghi, Nano Lett. **12**, 617 (2012).

[10] L. Gao, J. R. Guest, and N. P. Guisinger, Nano Lett. **10**, 3512 (2010).

[11] J. Xue, J. Sanchez-Yamagishi, D. Bulmash, P. Jacquod, A. Deshpande, K. Watanabe, T. Taniguchi, P. Jarrillo-Herrero, and B. J. LeRoy, Nat. Mater. **10**, 282 (2011).

[12] N. Levy, S. A. Burke, K. L. Meaker, M. Panlasigui, A. Zettl, F. Guinea, A. H. C. Neto, and M. F. Crommie, Science **329**, 544 (2010).

[13] C. N. Lau, W. Bao, and J. Velasco Jr., Mater. Today **15**, 238 (2012).

[14] A. Georgi, P. Nemes-Incze, R. Carrillo-Bastos, D. Faria, S. Viola Kusminskiy, D. Zhai, M. Schneider, D. Subramaniam, T. Mashoff, N. M. Freitag, M. Liebmann, M. Pratzer, L. Wirtz, C. R. Woods, R. V. Gorbachev, Y. Cao, K. S. Novoselov, N. Sandler, and M. Morgenstern, Nano Lett. **17**, 2240 (2017).

[15] Y. Wu, D. Zhai, C. Pan, B. Cheng, T. Taniguchi, K. Watanabe, N. Sandler, and M. Bockrath, Nano Lett. **18**, 64 (2018).

[16] A. Hewson, *The Kondo Problem to Heavy Fermions*, Cambridge Studies in Magnetism (Cambridge University Press, Cambridge, 1997).

[17] K. Sengupta and G. Baskaran, Phys. Rev. B **77**, 045417 (2008).

[18] Z.-G. Zhu, K.-H. Ding, and J. Berakdar, Europhys. Lett. **90**, 67001 (2010).

[19] B. Uchoa, T. G. Rappoport, and A. H. Castro Neto, Phys. Rev. Lett. **106**, 016801 (2011).

[20] D. Withoff and E. H. Fradkin, Phys. Rev. Lett. **64**, 1835 (1990).

[21] R. Bulla, T. Pruschke, and A. C. Hewson, J. Phys.: Condens. Matter **9**, 10463 (1997).

[22] C. Gonzalez-Buxton and K. Ingersent, Phys. Rev. B **57**, 14254 (1998).

[23] P. S. Cornaglia, G. Usaj, and C. A. Balseiro, Phys. Rev. Lett. **102**, 046801 (2009).

[24] B. Uchoa, L. Yang, S.-W. Tsai, N. M. R. Peres, and A. H. Castro Neto, Phys. Rev. Lett. **103**, 206804 (2009).

[25] L. Li, Y.-Y. Ni, Y. Zhong, T.-F. Fang, and H.-G. Luo, New J. Phys. **15**, 053018 (2013).

[26] L. Fritz and M. Vojta, Rep. Prog. Phys. **76**, 032501 (2013).

[27] J. Jobst, F. Kisslinger, and H. B. Weber, Phys. Rev. B **88**, 155412 (2013).

[28] P.-W. Lo, G.-Y. Guo, and F. B. Anders, Phys. Rev. B **89**, 195424 (2014).

[29] J. Hwang, K. Kim, H. Ryu, J. Kim, J.-E. Lee, S. Kim, M. Kang, B.-G. Park, A. Lanzara, J. Chung, S.-K. Mo, J. Denlinger, B. I. Min, and C. Hwang, Nano. Lett. **18**, 3661 (2018).

[30] J.-H. Chen, L. Li, W. G. Cullen, E. D. Williams, and M. S. Fuhrer, Nat. Phys. **7**, 535 (2011).

[31] R. R. Nair, M. Sepioni, I.-L. Tsai, O. Lehtinen, J. Keinonen, A. V. Krasheninnikov, T. Thomson, A. K. Geim, and I. V. Grigorieva, Nat. Phys. **8**, 199 (2012).

[32] J.-H. Chen, L. Li, W. G. Cullen, E. D. Williams, and M. S. Fuhrer, Nat. Phys. **8**, 353 (2012).

[33] Y. Jiang, P.-W. Lo, D. May, G. Li, G.-Y. Guo, F. B. Anders, T. Taniguchi, K. Watanabe, J. Mao, and E. Y. Andrei, Nat. Commun. **9**, 2349 (2018).

[34] D. May, P.-W. Lo, K. Deltenre, A. Henke, J. Mao, Y. Jiang, G. Li, E. Y. Andrei, G.-Y. Guo, and F. B. Anders, Phys. Rev. B **97**, 155419 (2018).

[35] H. C. Manohran, Bull. Am. Phys. Soc. **56**, P2.1 (2011).

[36] V. W. Brar, R. Decker, H.-M. Solowan, Y. Wang, L. Maserati, K. T. Chan, H. Lee, C. O. Girit, A. Zettl, S. G. Louie, M. L. Cohen, and M. F. Crommie, Nat. Phys. **7**, 43 (2011).

[37] H. González-Herrero, J. M. Gómez-Rodríguez, P. Mallet, M. Moaied, J. J. Palacios, C. Salgado, M. M. Ugeda, J.-Y. Veuillen, F. Yndurain, and I. Brihuega, Science **352**, 437 (2016).

[38] T. Eelbo, M. Waśniowska, M. Gyamfi, S. Forti, U. Starke, and R. Wiesendanger, Phys. Rev. B **87**, 205443 (2013).

[39] T. O. Wehling, H. P. Dahal, A. I. Lichtenstein, M. I. Katsnelson, H. C. Manoharan, and A. V. Balatsky, Phys. Rev. B **81**, 085413 (2010).

[40] H.-B. Z. Zhuan, Q.-F. Sun, and X. C. Xie, Europhys. Lett. **86**, 58004 (2009).

[41] V. G. Miranda, L. G. G. V. Dias da Silva, and C. H. Lewenkopf, Phys. Rev. B **90**, 201101(R) (2014).

[42] J. Ren, H. Guo, J. Pan, Y. Y. Zhang, X. Wu, H.-G. Luo, S. Du, S. T. Pantelides, and H.-J. Gao, Nano Lett. **14**, 4011 (2014).

[43] E. Voloshina, N. Berdunov, and Y. Dedkov, Sci. Rep. **6**, 20285 (2016).

[44] F. Guinea, M. I. Katsnelson, and A. K. Geim, Nat. Phys. **6**, 30 (2010).

[45] M. A. H. Vozmediano, M. I. Katsnelson, and F. Guinea, Phys. Rep. **496**, 109 (2010).

[46] M. Settnes, S. R. Power, M. Brandbyge, and A.-P. Jauho, Phys. Rev. Lett. **117**, 276801 (2016).

[47] S. P. Milovanović and F. M. Peeters, J. Phys.: Condens. Matter **29**, 075601 (2017).

[48] S. Viola Kusminskiy, D. K. Campbell, A. H. Castro Neto, and F. Guinea, Phys. Rev. B **83**, 165405 (2011).

[49] M. Neek-Amal and F. M. Peeters, Phys. Rev. B **85**, 195445 (2012).

[50] R. Carrillo-Bastos, D. Faria, A. Latgé, F. Mireles, and N. Sandler, Phys. Rev. B **90**, 041411(R) (2014).

[51] M. Schneider, D. Faria, S. Viola Kusminskiy, and N. Sandler, Phys. Rev. B **91**, 161407(R) (2015).

[52] R. Carrillo-Bastos, C. León, D. Faria, A. Latgé, E. Y. Andrei, and N. Sandler, Phys. Rev. B **94**, 125422 (2016).

[53] L. D. Landau, L. P. Pitaevskii, A. M. Kosevich, and E. M. Lifshitz, *Theory of Elasticity: Volume 7 (Course of Theoretical Physics)* (Butterworth-Heinemann, Oxford, 2012).

[54] A. L. Kitt, V. M. Pereira, A. K. Swan, and B. B. Goldberg, Phys. Rev. B **85**, 115432 (2012).

[55] A. L. Kitt, V. M. Pereira, A. K. Swan, and B. B. Goldberg, Phys. Rev. B **87**, 159909(E) (2013).

[56] V. M. Pereira, A. H. Castro Neto, and N. M. R. Peres, Phys. Rev. B **80**, 045401 (2009).

[57] D. Midtvedt, C. H. Lewenkopf, and A. Croy, 2D Mater. **3**, 011005 (2016).

[58] C. W. J. Beenakker, Rev. Mod. Phys. **80**, 1337 (2008).

[59] H. Suzuura and T. Ando, Phys. Rev. B **65**, 235412 (2002).

[60] J. V. Sloan, A. A. P. Sanjuan, Z. Wang, C. Horvath, and S. Barraza-Lopez, Phys. Rev. B **87**, 155436 (2013).

[61] S.-M. Choi, S.-H. Jhi, and Y.-W. Son, Phys. Rev. B **81**, 081407(R) (2010).

[62] Y. Zhang, M. Heiranian, B. Janicek, Z. Budrikis, S. Zapperi, P. Y. Huang, H. T. Johnson, N. R. Aluru, J. W. Lyding, and N. Mason, Nano Lett. **18**, 2098 (2018).

[63] D. Nelson, T. Piran, and S. Weinberg, *Statistical Mechanics of Membranes and Surfaces* (World Scientific, Singapore, 2004).

[64] C. L. Kane and E. J. Mele, Phys. Rev. Lett. **78**, 1932 (1997).

[65] E.-A. Kim and A. H. Castro Neto, Europhys. Lett. **84**, 57007 (2008).

[66] F. de Juan, M. Sturla, and M. A. H. Vozmediano, Phys. Rev. Lett. **108**, 227205 (2012).

[67] G. G. Naumis, S. Barraza-Lopez, M. Oliva-Leyva, and H. Terrones, Rep. Prog. Phys. **80**, 096501 (2017).

[68] M. Oliva-Leyva and G. G. Naumis, Phys. Lett. A **379**, 2645 (2015).

[69] M. Oliva-Leyva, J. E. Barrios-Vargas, and C. Wang, J. Phys.: Condens. Matter **30**, 085702 (2018).

[70] E. N. Economou, *Green's Functions in Quantum Physics*, Springer Series in Solid-State Sciences (Springer, Berlin, 2006).

[71] A. Ferreira, J. Viana-Gomes, J. Nilsson, E. R. Mucciolo, N. M. R. Peres, and A. H. Castro Neto, Phys. Rev. B **83**, 165402 (2011).

[72] R. Mozara, M. Valentyuk, I. Krivenko, E. Şaşıoğlu, J. Kolorenč, and A. I. Lichtenstein, Phys. Rev. B **97**, 085133 (2018).

[73] Y. Virgus, W. Purwanto, H. Krakauer, and S. Zhang, Phys. Rev. Lett. **113**, 175502 (2014).

[74] T. Eelbo, M. Waśniowska, P. Thakur, M. Gyamfi, B. Sachs, T. O. Wehling, S. Forti, U. Starke, C. Tieg, A. I. Lichtenstein, and R. Wiesendanger, Phys. Rev. Lett. **110**, 136804 (2013).

[75] M. Gyamfi, T. Eelbo, M. Waśniowska, T. O. Wehling, S. Forti, U. Starke, A. I. Lichtenstein, M. I. Katsnelson, and R. Wiesendanger, Phys. Rev. B **85**, 161406(R) (2012).

[76] D. A. Ruiz-Tijerina and L. G. G. V. Dias da Silva, Phys. Rev. B **94**, 085425 (2016).

[77] D. A. Ruiz-Tijerina and L. G. G. V. Dias da Silva, Phys. Rev. B **95**, 115408 (2017).

[78] F. D. M. Haldane, J. Phys. C: Solid State Phys. **11**, 5015 (1978).

[79] K. G. Wilson, Rev. Mod. Phys. **47**, 773 (1975).

[80] H. R. Krishna-murthy, J. W. Wilkins, and K. G. Wilson, Phys. Rev. B **21**, 1003 (1980).

[81] H. R. Krishna-murthy, J. W. Wilkins, and K. G. Wilson, Phys. Rev. B **21**, 1044 (1980).

[82] R. Bulla, T. A. Costi, and T. Pruschke, Rev. Mod. Phys. **80**, 395 (2008).

[83] M. Cheng, T. Chowdhury, A. Mohammed, and K. Ingersent, Phys. Rev. B **96**, 045103 (2017).